



Cite this: *Phys. Chem. Chem. Phys.*,  
2024, 26, 14345

# <sup>1</sup>H and <sup>13</sup>C chemical shift–structure effects in anhydrous $\beta$ -caffeine and four caffeine–diacid cocrystals probed by solid-state NMR experiments and DFT calculations<sup>†</sup>

Debashis Majhi,<sup>‡</sup> Baltzar Stevensson,<sup>ID</sup> Tra Mi Nguyen and Mattias Edén<sup>ID\*</sup>

By using density functional theory (DFT) calculations, we refined the H atom positions in the structures of  $\beta$ -caffeine (C),  $\alpha$ -oxalic acid (OA; (COOH)<sub>2</sub>),  $\alpha$ -(COOH)<sub>2</sub>·2H<sub>2</sub>O,  $\beta$ -malonic acid (MA),  $\beta$ -glutaric acid (GA), and  $\text{I}$ -maleic acid (ME), along with their corresponding cocrystals of 2:1 (2C–OA, 2C–MA) or 1:1 (C–GA, C–ME) stoichiometry. The corresponding <sup>13</sup>C/<sup>1</sup>H chemical shifts obtained by gauge including projector augmented wave (GIPAW) calculations agreed overall very well with results from magic-angle-spinning (MAS) nuclear magnetic resonance (NMR) spectroscopy experiments. Chemical-shift/structure trends of the precursors and cocrystals were examined, where good linear correlations resulted for all COO<sup>1</sup>H sites against the H···O and/or H···N H-bond distance, whereas a general correlation was neither found for the aliphatic/caffeine-stemming <sup>1</sup>H sites nor any <sup>13</sup>C chemical shift against either the intermolecular hydrogen- or tetrel-bond distance, except for the <sup>13</sup>COOH sites of the 2C–OA, 2C–MA, and C–GA cocrystals, which are involved in a strong COOH···N bond with caffeine that is responsible for the main supramolecular stabilization of the cocrystal. We provide the first complete <sup>13</sup>C NMR spectral assignment of the structurally disordered anhydrous  $\beta$ -caffeine polymorph. The results are discussed in relation to previous literature on the disordered  $\alpha$ -caffeine polymorph and the ordered hydrated counterpart, along with recommendations for NMR experimentation that will secure sufficient <sup>13</sup>C signal-resolution for reliable resonance/site assignments.

Received 20th December 2023,

Accepted 8th April 2024

DOI: 10.1039/d3cp06197c

rsc.li/pccp

## 1 Introduction

Efficient administration of active pharmaceutical ingredients (APIs) is often challenging because the powders are either unstable or feature a low solubility in water/body fluids. One option for improving the solubility and/or other physical or chemical properties without recourse to ionic salts is the usage of a *cocrystal*, *i.e.*, a supramolecular compound of an API and another molecular species (or even another API, a so-called drug–drug cocrystal).<sup>1–3</sup> Consequently, intense efforts have been spent during the past two decades to explore synthetic routes to cocrystal preparation as well as their structures and formation mechanisms.<sup>2–5</sup>

One widely used API is the stimulant caffeine (1,3,7-trimethylpurine-2,6-dione), whose storage and precise quantitative (physiological) administration is complicated by its

highly hygroscopic nature.<sup>6–8</sup> At room temperature (RT) in the absence of humidity, anhydrous caffeine exists as the low-temperature “ $\beta$ ” modification, which at temperatures  $>150$  °C converts into the metastable high-temperature “ $\alpha$ ” form, which transforms very slowly into  $\beta$ -caffeine at RT and dry air.<sup>9</sup> Hence, commercial anhydrous caffeine powders often comprise a mixture of both modifications. Caffeine also exists in a monohydrate form, which unfortunately is very unstable at RT and converts either into phases with  $<1$  water molecule/caffeine moiety or anhydrous  $\beta$ -caffeine (depending on the relative humidity).<sup>7,9</sup> Hence, large-scale storage, processing and other handling of caffeine powder with a well-defined stoichiometry is not trivial.

Yet, as demonstrated by Trask *et al.*,<sup>8</sup> cocrystals of caffeine with diacids, such as oxalic acid (OA), malonic acid (MA), glutaric acid (GA), and maleic acid (ME), are stable across wide humidity ranges. Several studies are reported on their formation, stability, and physical properties.<sup>8,10–14</sup> The present investigation targeted the cocrystal structures obtained from  $\beta$ -caffeine ( $\beta$ -C) with each of OA, MA, GA, and ME, abbreviated as 2C–OA, 2C–MA, C–GA, and C–ME, respectively, according to the corresponding 2:1 and 1:1 caffeine:diacid stoichiometry.

Department of Materials and Environmental Chemistry, Stockholm University, SE-106 91, Stockholm, Sweden. E-mail: mattias.eden@mmk.su.se

<sup>†</sup> Electronic supplementary information (ESI) available. See DOI: <https://doi.org/10.1039/d3cp06197c>

<sup>‡</sup> Present address: Department of Chemistry, National Institute of Technology Tiruchirappalli, Tiruchirappalli-620015, Tamil Nadu, India.



Although a fixed stoichiometry would be desirable, the C-ME cocrystal is metastable,<sup>10</sup> while 2C-OA, 2C-MA, and C-GA cocrystals were hitherto not reported. Each X-ray diffraction (XRD) derived cocrystal structure is reported,<sup>8</sup> encompassing the main caffeine–diacid motifs governing their supramolecular organization *via* hydrogen bonds (Section 3). The well-known limitation of XRD to locate precise H-atom positions, however, restricts its capacity of unveiling quantitative details on weak non-covalent interactions, such as H···O/N hydrogen and C···O/N tetrel bonds that account for the intermolecular interactions and structural organization of cocrystals, as well as numerous other supramolecular systems. Then, high-resolution magic-angle-spinning (MAS) <sup>1</sup>H and <sup>13</sup>C nuclear magnetic resonance (NMR) spectroscopy offer valuable complementary structural insight,<sup>15–20</sup> in particular for structurally disordered (in)organic phases,<sup>18,20,21</sup> encompassing  $\beta$ -caffeine.<sup>14,22–24</sup>

Herein, we present a comprehensive combined MAS NMR and density functional theory (DFT) study, reporting on DFT refinements of previous XRD-derived structures of each 2C-OA, 2C-MA, C-GA, and C-ME cocrystal<sup>8</sup> together with each  $\beta$ -caffeine,<sup>9</sup>  $\alpha$ -OA,<sup>25</sup>  $\alpha$ -OA·2H<sub>2</sub>O,<sup>26</sup>  $\beta$ -MA,<sup>27</sup>  $\beta$ -GA,<sup>28</sup> and I-ME<sup>29</sup> precursor phase. <sup>1</sup>H and <sup>13</sup>C isotropic chemical shifts calculated by the gauge including projector augmented wave (GIPAW) method<sup>30–33</sup> were contrasted with those from MAS NMR experiments, aiming at improved insight into the shift-structure trends, notably the *hydrogen bond* (HB)<sup>34–46</sup>—and for the methyl moieties also *tetrel bond* (TB)<sup>47–49</sup>—effects on the chemical shifts. While the complete sets of <sup>13</sup>C chemical shifts/NMR-peak assignments of the 2C-MA and C-GA cocrystals were reported earlier by Vigilante and Mehta,<sup>50</sup> out of the four cocrystals considered herein, a majority of the <sup>1</sup>H chemical shifts are reported for the first time, along with nearly half of their <sup>13</sup>C counterparts, such as those for 2C-OA and C-ME. We also present the first complete <sup>13</sup>C NMR spectral assignment of the ten resonances from the eight unique <sup>13</sup>C sites of the structurally disordered anhydrous  $\beta$ -caffeine polymorph. The results are discussed in relation to previous <sup>13</sup>C MAS NMR reports on the ordered hydrated and anhydrous disordered  $\alpha$ / $\beta$ -caffeine and polymorphs, highlighting the role of the magnetic field for unambiguously discriminating between the  $\alpha$ - and  $\beta$ -caffeine forms.

## 2 Materials and Methods

### 2.1 Cocrystal preparation

Anhydrous  $\beta$ -caffeine (98% purity), oxalic acid (98%), malonic acid (99%), glutaric acid (99%) and chloroform were obtained from Sigma-Aldrich along with maleic acid (99%) from Thermo Fisher. All cocrystals were prepared by solvent drop grinding,<sup>8,13</sup> using ball milling (Mixer Mill 500 Vario; Retsch) of the two precursor powders that were placed in a 25 mL stainless steel jar and ground with 7 mm stainless steel balls at a rate of 30 Hz for 90 min. All cocrystals were prepared from stoichiometric amounts of the precursors. The 2C-OA (space group *P*2<sub>1</sub>/c) and

2C-MA (*F*dd2) cocrystals<sup>8</sup> with a 2:1 caffeine:diacid stoichiometry resulted by mixing 250 mg of  $\beta$ -caffeine with either 60 mg of  $\alpha$ -OA or 70 mg of  $\beta$ -MA, respectively, along with 5 drops of chloroform. Likewise, the 1:1 stoichiometric C-GA (form II;<sup>8</sup> space group *P*1) cocrystal was prepared by grinding 510 mg of  $\beta$ -caffeine with 350 mg of  $\beta$ -GA and a few drops of chloroform, and likewise for the C-ME (*P*2<sub>1</sub>/n) counterpart (250 mg of  $\beta$ -MA and 150 mg of I-ME).<sup>8</sup>

### 2.2 Powder X-ray diffraction

Powder XRD (PXRD) patterns were collected from all cocrystals and precursors with a Bruker D8 Discover diffractometer equipped with a LYNXEYE position-sensitive detector, using Cu  $K\alpha_{1,2}$  radiation ( $\lambda_1 = 154.06$  pm;  $\lambda_2 = 154.44$  pm) and a focusing Göbel mirror. Each powder was filled in a 0.7 mm borosilicate glass capillary. All diffractograms were collected at RT over a  $2\theta$  range of 5°–50°, employing a step size of 0.02° with either 0.25 s per step (for  $\beta$ -caffeine, OA,  $\beta$ -MA,  $\beta$ -GA, I-ME, 2C-MA, and C-ME) or 0.75 s per step (for 2C-OA and C-GA), giving total measurement times of around 10 and 30 min per sample, respectively. The XRD patterns of the precursors and cocrystals are shown in Fig. S1 and S2 (ESI†), respectively. Rietveld refinements and Pawley fits, performed with the TOPAS software,<sup>51</sup> verified a near-100% purity of all specimens, except for the oxalic acid powder, which comprised a mixture of  $\alpha$ -OA (96.1 wt%),  $\alpha$ -OA·2H<sub>2</sub>O (3.5%), and  $\beta$ -OA (0.39 wt%). The anhydrous  $\beta$ -caffeine purity was  $\geq 99.6\%$ , along with a (statistically unascertained) minute amount of  $\alpha$ -caffeine (0.37 wt%). All refined unit cell parameters are listed in Table S1 (ESI†).

### 2.3 Solid-state NMR

All solid-state NMR experiments were performed at ambient temperature with a Bruker Avance-III spectrometer and a magnetic field ( $B_0$ ) of 14.1 T, which provided the respective <sup>1</sup>H and <sup>13</sup>C Larmor frequencies of  $-600.1$  MHz and  $-150.9$  MHz. <sup>1</sup>H and <sup>13</sup>C chemical shifts are quoted relative to neat tetramethylsilane (TMS).

<sup>1</sup>H → <sup>13</sup>C cross polarization (CP) MAS NMR (CPMAS) experimentation was performed with filled 4.0 mm zirconia rotors spinning at the MAS rate ( $\nu_r$ ) of 12.00 kHz, using contact periods ( $\tau_{CP}$ ) of 1.25 ms (except for  $\beta$ -MA; 833  $\mu$ s and  $\nu_r = 9.00$  kHz), and the modified Hartmann–Hahn condition  $\nu_H = \nu_C + \nu_r$ , where the <sup>13</sup>C nutation frequency ( $\nu_C$ ) was ramped linearly<sup>52</sup> by  $\pm 4.7$  kHz around  $\nu_C = 47$  kHz. Throughout, the 90° <sup>1</sup>H pulse prior to CP operated at  $\nu_H \approx 100$  kHz and SPINAL-64<sup>53</sup> proton decoupling at  $\nu_H \approx 78$  kHz (6.4  $\mu$ s pulses) was applied during signal detection. The relaxation delays ( $\tau_{relax}$ ) varied between 15 s and 30 s. The signal averaging involved 2048–3328 co-added signal transients, except for MA and GA (1024). Single-pulse (“Bloch decay”) <sup>1</sup>H MAS NMR spectra were recorded with 1.3 mm zirconia rotors undergoing fast MAS at 60.00 kHz with 90° rf pulses operating at the <sup>1</sup>H nutation frequency  $\nu_H \approx 80$  kHz. 256–512 accumulated NMR-signal transients were recorded with  $\tau_{relax} = 3$  s. These relaxation delays were not sufficiently long to ensure NMR intensities



that quantitatively reflect the relative H/C site populations in the structures but do not affect any conclusions from our analysis, which only concerned the chemical shifts. NMR spectral deconvolutions were performed with in-house developed software.<sup>54</sup>

## 2.4 DFT/GIPAW calculations

DFT energy optimizations were performed on the following published PXRD-derived structures:  $\beta$ -caffeine;<sup>9</sup>  $\alpha$ -OA;<sup>25</sup>  $\alpha$ -OA-2H<sub>2</sub>O;<sup>26</sup>  $\beta$ -MA;<sup>27</sup>  $\beta$ -GA;<sup>28</sup> I-ME,<sup>29</sup> whereas all cocrystal structures were from ref. 8; see Table S2 (ESI<sup>†</sup>). The first-principle DFT energy minimizations were performed with the CASTEP software<sup>55</sup> (version 22.11) along current standard and well-developed protocols,<sup>19,32,33</sup> encompassing usage of the local density approximation (LDA) functional<sup>56</sup> with on-the-fly-generated ultrasoft pseudopotentials<sup>57</sup> and a plane-wave basis set.<sup>58</sup> The Tkatchenko and Scheffler method was employed for dispersion corrections.<sup>59</sup> All structures were initially optimized by solely adjusting the proton positions with fixed positions of all heavier atoms and unit-cell parameters. However, the agreement between the experimental and GIPAW-derived chemical shifts improved slightly for the  $\beta$ -caffeine structure by optimizing *all* cell parameters and atom positions (Table S2 and Section 4.3, ESI<sup>†</sup>). The <sup>1</sup>H and <sup>13</sup>C magnetic shielding values were calculated with the GIPAW method<sup>19,30–33</sup> for all DFT-optimized structures. For both the DFT energy optimizations and the GIPAW shielding-parameter calculations, a Monkhorst–Pack *k*-point grid<sup>60</sup> was used with a maximum spacing of 0.05 Å<sup>–1</sup> in the reciprocal space, and a 1000 eV plane-wave energy cutoff to ensure convergence.

The DFT/GIPAW-derived principal values,  $\{\sigma_{xx}^{Hj}, \sigma_{yy}^{Hj}, \sigma_{zz}^{Hj}\}$  and  $\{\sigma_{xx}^{Cj}, \sigma_{yy}^{Cj}, \sigma_{zz}^{Cj}\}$ , of the respective second-rank magnetic shielding tensor of each unique <sup>1</sup>H<sub>j</sub> and <sup>13</sup>C<sub>j</sub> site in the structure were converted into the corresponding chemical shift values,  $\{\delta_{xx}^{Sj}, \delta_{yy}^{Sj}, \delta_{zz}^{Sj}\}$ , by the expression<sup>19,32,33</sup>

$$\delta_{\alpha\alpha}^{Sj} = \sigma_{\text{ref}}^S - \sigma_{\alpha\alpha}^{Sj}, \quad \text{with } \alpha\alpha = \{xx, yy, zz\} \text{ and } S = \{^1\text{H}, ^{13}\text{C}\}. \quad (1)$$

We employ a chemical shift scale throughout, where low (high) chemical shifts correspond to shielded (deshielded) nuclei, and the *isotropic chemical shift* is given by<sup>61–63</sup>

$$\delta_S^j \equiv \delta_S^{\text{iso},j} = \frac{1}{3}(\delta_{xx}^{Sj} + \delta_{yy}^{Sj} + \delta_{zz}^{Sj}) \quad \text{for } S = \{^1\text{H}, ^{13}\text{C}\}. \quad (2)$$

The shielding-to-shift conversion terms of eqn (1) were  $\sigma_{\text{ref}}^{\text{H}} = 29.034$  ppm for <sup>1</sup>H and  $\sigma_{\text{ref}}^{\text{C}} = 169.837$  ppm for <sup>13</sup>C. The values were obtained by linear regressions that minimized the difference between the sets of calculated and experimental isotropic <sup>1</sup>H and <sup>13</sup>C chemical shifts based on roughly half of each entire set of  $\{\delta_{\text{H}}^j\}$  and  $\{\delta_{\text{C}}^j\}$  values, and giving correlation coefficients ( $R^2$ ) of  $R^2 = 0.980$  and  $R^2 = 0.999$  when evaluated across each entire  $\{\delta_{\text{H}}^j\}$  and  $\{\delta_{\text{C}}^j\}$  ensemble, respectively.

## 3 Overview of cocrystals and their precursor structures

Fig. 1 shows the structures of caffeine and the four diacid molecules, where each number represents the <sup>13</sup>C site index, giving the label “C<sub>j</sub>” with  $1 \leq j \leq 22$ , while all its directly bonded H, O, and N atoms carry the same index  $j$ . Note that although the C14/C18 sites are crystallographically equivalent in the  $\beta$ -GA structure, they are *inequivalent* in the C-GA cocrystal. For simplicity, we employ a strict C1–C22 labelling because all C/H sites are crystallographically distinct in either/both the diacid/cocrystal structure, except for C9/C10 (H9/H10), which remain equivalent in each  $\alpha$ -OA,  $\alpha$ -OA-2H<sub>2</sub>O, and 2C-OA structure.

Fragments from the by DFT energy-minimized crystal structures (Section 2.4) are shown in Fig. 2 for the diacids (a, b, d, f, h) and their respective cocrystals with caffeine (c, e, g, i). All

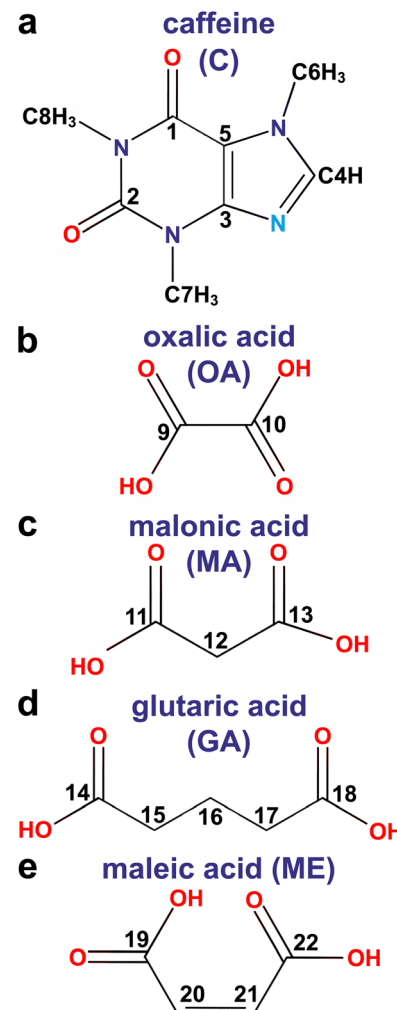


Fig. 1 Molecular structure with atom numbering of (a) caffeine, and the (b) oxalic, (c) malonic, (d) glutaric, and (e) maleic diacids. Each label/index  $j$  refers to carbon atom “C<sub>j</sub>”, whose directly bonded O, N, and H atoms feature the same label (O<sub>j</sub>, N<sub>j</sub>, and H<sub>j</sub>, respectively), except for the nitrogen atom of the imidazolium ring (cyan color) in (a), which is referred to simply as “N”.

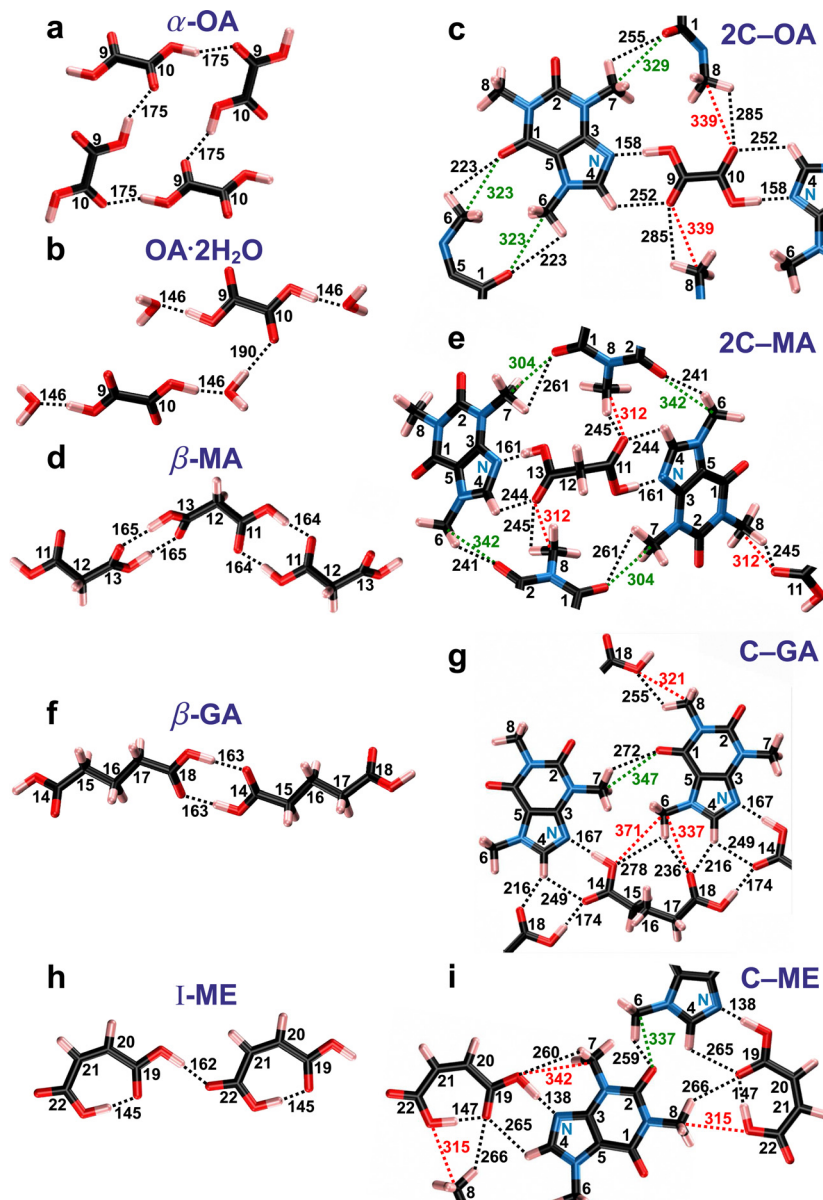


Fig. 2 Fragments from the DFT-refined crystal structures of (a)  $\alpha$ -OA, (b)  $\alpha$ -OA·2H<sub>2</sub>O, (c) 2C-OA, (d)  $\beta$ -MA, (e) 2C-MA, (f)  $\beta$ -GA, (g) C-GA, (h) I-ME, and (i) C-ME. The dotted lines mark intermolecular H and tetrel bonds, with the accompanying number specifying the distance (in pm). The red and green lines/numbers distinguish tetrel bonds between caffeine-diacid and caffeine-caffiene molecules, respectively. Note that each methyl group undergoes a rapid rotation around the C-N bond and that only one H bond is indicated for each of the three equivalent protons.

pristine diacid structures involve strong intermolecular H bonds between the carboxy groups of neighboring molecules, except for I-ME, which besides one expected C19OOH···O22 contact also features a short *intramolecular* C22OOH···O19 HB (Fig. 2h), which remains intact also in the C-ME cocrystal shown in Fig. 2i, within a minute (2 pm) lengthening.

As discussed by Trask *et al.*,<sup>8</sup> both 2C-OA and 2C-MA cocrystals feature a heteromeric synthon where one diacid molecule is sandwiched between two caffeine units by a strong COOH···N hydrogen bond and a weaker C4H···OOC counterpart (Fig. 2c and e). The alternating caffeine-diacid-caffiene moieties of the supramolecular structure are stabilized

primarily by those H bonds.<sup>8</sup> The 1:1 caffeine:diacid stoichiometries of C-GA and C-ME, however, yield different intermolecular interactions. Owing to the intact *intramolecular* C22H···O19 bond in the C-ME cocrystal (Fig. 2i), its structure involves strictly alternating caffeine-ME interconnections, with a similar C4H···O19OC and C19OOH···N bond constellation as in the 2C-OA/MA cocrystals, *yet* with only *one* diacid-COOH group H-bonded to caffeine. Moreover, while the C-GA structure is also stabilized by two N···H14OOC and C4H···O14OC bonds between caffeine and one GA molecule (Fig. 2g), the C4H atom *also* involves another HB with O18 of a second diacid molecule, where moreover C18H is bonded to O14 of the first



diacid unit. Hence, each caffeine molecule in C-GA features three different H bonds to two distinct GA molecules, both of which are additionally interlinked by a HB between their carboxy moieties, as in the parent GA structure.

Although the  $\text{N}\cdots\text{H}$  bond between caffeine and a COOH group of a diacid unit constitutes the strongest intermolecular contact of the cocrystal,<sup>8</sup> a further minor structure stabilization is arranged by H bonds between the  $\text{CH}_3$  groups of caffeine with *either* diacid carboxy moieties *or* the O1/O2 atoms of neighboring caffeine molecules (Fig. 2c, e, g and i). The  $\text{CH}_3$  moieties may furthermore form weak  $\text{CH}_3\cdots\text{O}$  tetrel bonds<sup>47–49</sup> with the O1/O2 atoms of caffeine, or with the CO counterparts of the diacids, as marked in green and red color, respectively, in Fig. 2c, e, g and i (see Section 4.7). The methyl groups also form intermolecular tetrel and H bonds in the structurally disordered  $\beta$ -caffeine structure (Table S3, ESI†). We refer to ref. 9 and 22 for details about the anhydrous  $\beta$ -caffeine structure, whose unit cell comprises five inequivalent molecules, and thereby five NMR signal-contributions to each detected  $^{13}\text{C}$  and  $^1\text{H}$  resonance.

## 4 Results and discussion

### 4.1. $^{13}\text{C}$ MAS NMR spectra from cocrystal precursors

Because the chemical shift of a given  $^{13}\text{C}$  or  $^1\text{H}$  nuclear site reflects its electronic environment in the structure, it is often a sensitive probe of the precise location of neighboring atoms in close vicinity. Fig. 3 displays the  $^{13}\text{C}$  CPMAS NMR spectra recorded from the diacids and  $\beta$ -caffeine cocrystal precursors. They involve resonances ranging from the most deshielded  $^{13}\text{C}$  nuclei (high chemical shifts) of carboxy groups with  $\delta_{\text{C}} \gtrsim 160$  ppm from the diacids (Fig. 3a–d) to the more shielded (lower shifts) aliphatic  $^{13}\text{C}$  sites with chemical shifts  $\delta_{\text{C}} \lesssim 40$  ppm from  $\beta$ -MA,  $\beta$ -GA, and  $\beta$ -caffeine (Fig. 3b, c and e). The NMR spectral region intermediate of these extreme  $^{13}\text{C}$  shifts encompasses the comparatively deshielded  $^{13}\text{C}$ 20 and  $^{13}\text{C}$ 21 sites of I-ME (Fig. 3d), together with the  $^{13}\text{C}$ 1– $^{13}\text{C}$ 5 sites of  $\beta$ -caffeine resonating between 105–155 ppm (Fig. 3e).

All cocrystal precursor powders (but OA) were phase pure, where the two crystallographically inequivalent  $^{13}\text{COOH}$  sites of MA and ME reveal chemical-shift differences of 0.4 ppm and 3.7 ppm, respectively, while both  $^{13}\text{COOH}$  sites of GA resonate at 181.5 ppm. In contrast, the two  $^{13}\text{C}$  NMR signals at 160.7 ppm and 163.1 ppm from OA derive from anhydrous  $\alpha$ -OA and  $\alpha$ -OA·2H<sub>2</sub>O, respectively, each featuring one crystallographically unique  $^{13}\text{COOH}$  site.<sup>25,26</sup> From the integrated  $^{13}\text{C}$  NMR intensities of Fig. 3a, and confirmed by integrating the corresponding  $^1\text{H}$  MAS NMR spectrum (Section 4.5.1), we estimated relative OA:OA·2H<sub>2</sub>O amounts of approximately 0.7:1.0 in the oxalic acid mixture. (Although that estimate is only approximate, its precise value is immaterial for our subsequent analyses. The reason for the markedly higher OA·2H<sub>2</sub>O content derived by NMR relative to PXRD is unknown but likely stems from a water uptake of the OA powder prior to the NMR experiments). The  $^{13}\text{C}$  chemical shifts obtained from Fig. 3

agree well with previous reports from  $\alpha$ -OA,<sup>36,64</sup>  $\alpha$ -OA·2H<sub>2</sub>O,<sup>36</sup> MA,<sup>14,65</sup> GA,<sup>36,65,66</sup> and ME.<sup>65–67</sup>

### 4.2. $^{13}\text{C}$ NMR-peak assignments of anhydrous $\beta$ -caffeine

Notwithstanding several  $^{13}\text{C}$  NMR publications on caffeine-based cocrystals,<sup>23,24,41,46,49,50</sup> encompassing complete  $\{\delta_{\text{C}}\}$  reports thereof,<sup>23,50</sup> ambiguities prevail about the precise set of  $^{13}\text{C}$  shifts and their assignments of the anhydrous  $\beta$ -caffeine structure *itself*, which produces two hitherto unassigned  $^{13}\text{C}$  resonances, none of which are present in MAS NMR spectra from either the structurally ordered caffeine monohydrate (henceforth referred to as C-H<sub>2</sub>O) or disordered anhydrous  $\alpha$ -caffeine modifications,<sup>22</sup> each of which manifests one  $^{13}\text{C}$  resonance per C1–C8 site. Enright *et al.*<sup>22</sup> presented  $^{13}\text{C}$  MAS NMR spectra from all  $\alpha$ -/  $\beta$ -caffeine and C-H<sub>2</sub>O forms, but precise chemical shifts were only reported for the latter.<sup>22</sup> Likewise,  $\delta_{\text{C}}$  values were not provided along with the  $^{13}\text{C}$  MAS NMR spectra from the anhydrous caffeine modifications studied in ref. 12, 24, 50 and 68. To the best of our knowledge, Table 1 presents the precise  $^{13}\text{C}$  chemical shifts *and* complete peak assignments for the anhydrous  $\beta$ -caffeine polymorph for the first time, where all further references herein to “ $\alpha$ -/  $\beta$ -caffeine” imply the anhydrous polymorphs. The  $^{13}\text{C}$  MAS NMR spectrum from  $\beta$ -caffeine of Fig. 3e appears to match very well that reported in ref. 22 while moreover our PXRD analysis confirmed a phase-pure specimen (Section 2.2). Notwithstanding that all eight  $\{\delta_{\text{C}}^{\text{a}}\}$  values of both  $\alpha$ -/  $\beta$ -caffeine modifications are (very) similar,<sup>22</sup> the presence of two additional  $^{13}\text{C}$  NMR peaks at 149 ppm and 30 ppm in  $\beta$ -caffeine (Fig. 3e) distinguishes it from its “ $\alpha$ ” and C-H<sub>2</sub>O counterparts, which Enright *et al.*<sup>22</sup> attributed to  $^{13}\text{C}$  sites of crystallographically distinct molecules in the  $\beta$ -caffeine unit cell. That very plausible suggestion is confirmed below.

Previous solid-state  $^{13}\text{C}$  NMR-peak assignments of all anhydrous and monohydrate caffeine polymorphs derive either from (i) employing DFT/GIPAW calculations of a caffeine-based cocrystal to assign its  $^{13}\text{C}$  sites of the caffeine moiety<sup>23,24,50</sup> or from (ii) the solution-NMR work of Sitkowski *et al.*,<sup>69</sup> which was exploited by Enright *et al.*<sup>22</sup> for the  $^{13}\text{C}$ -site/ NMR-peak identifications of the ordered C-H<sub>2</sub>O modification in the solid state (which is greatly facilitated by its narrow  $^{13}\text{C}$  resonances). Those peak assignments were subsequently assumed in ref. 14 and 70. Although such straightforward  $^{13}\text{C}$  site/shift-mappings are also sufficiently reliable for application to  $\alpha$ -caffeine, which involves one resonance per  $^{13}\text{C}$  site, the peak-assignment strategies (i) and (ii) are precluded for the two additional resonances at around 149/30 ppm from  $\beta$ -caffeine and labelled as C3'/C78 in Fig. 3e. To the best of our knowledge, both remain unidentified in current literature. Nonetheless, for each  $^{13}\text{C}$ 1– $^{13}\text{C}$ 8 resonance assignment of Fig. 3e, the DFT/GIPAW-derived  $^{13}\text{C}$  chemical shifts of Table 1 corroborate previously employed NMR-peak assignments made for both C-H<sub>2</sub>O and  $\alpha$ -caffeine modifications.<sup>14,22–24,70</sup> The modeled chemical shifts, which were averaged over the 5 distinct caffeine molecules in the unit cell, reproduce the  $^{13}\text{C}$  NMR results from  $\beta$ -caffeine (very) well (Table 1), which for every asymmetric peakshape represents the *center-of-gravity* (CG) shift ( $\bar{\delta}_{\text{C}}$ ) obtained from NMR-peak deconvolutions into two components



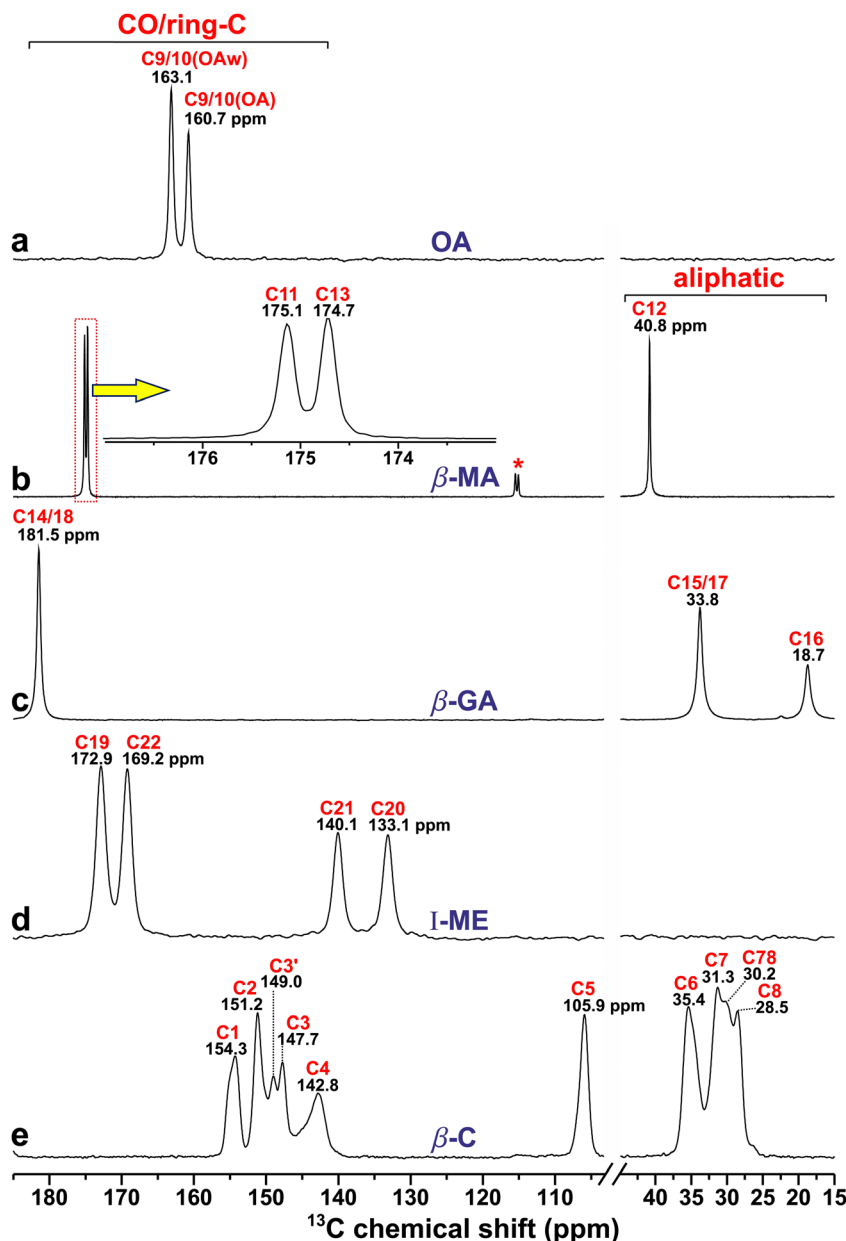


Fig. 3  $^{13}\text{C}$  CPMAS NMR spectra recorded at 14.1 T and a MAS rate of 12.00 kHz from (a)  $\alpha$ -OA/ $\alpha$ -OA- $2\text{H}_2\text{O}$  mixture ("OA"), (b) malonic acid ( $\beta$ -MA), (c) glutaric acid ( $\beta$ -GA), (d) maleic acid (I-ME), and (e) anhydrous  $\beta$ -caffeine ( $\beta$ -C). Here and in other figures: NMR signals from the  $\alpha$ -OA and  $\alpha$ -OA- $2\text{H}_2\text{O}$  phases are abbreviated by "OA" and "OA<sub>w</sub>", respectively, whereas the red and black number above each NMR peak marks the C label of Fig. 1 and the chemical shift (in ppm) at the peak maximum, respectively. The inset of (b) is a zoom of the NMR spectral region marked by the dotted rectangle, and the asterisk marks a spinning sideband from the use of a lower MAS rate (9.00 kHz) for this experiment.

(Fig. S3, ESI<sup>†</sup>) rather than the shift at the peak-maximum amplitude ( $\delta_{\text{C}}$ ). Note that (I)  $\bar{\delta}_{\text{C}}$  and  $\delta_{\text{C}}$  represent the *average* and the *most probable* value over the chemical-shift distribution of  $^{13}\text{C}_j$ , respectively; (II) invoking CG shifts is only required for the structurally disordered  $\beta$ -caffeine structure, as opposed to those of any cocrystal or diacid precursor considered herein, for which  $\bar{\delta}_{\text{C}} = \delta_{\text{C}}$  throughout.

Despite an overall good agreement between the experimental and modeled  $^{13}\text{C}$  chemical shifts of  $\beta$ -caffeine, the DFT/GIPAW calculations alone *cannot uniquely* identify the hitherto unassigned resonances at 149.0 ppm and 30.2 ppm

(Fig. 3e). By spectral deconvolution, however, the integrated  $^{13}\text{C}$  NMR-peak intensities at around {154.3, 151.2, 149.0, 147.7} ppm were found to relate as 1.00:1.44:0.27:0.74 (Fig. S3, ESI<sup>†</sup>). That observation naturally attributes the resonance at 149.0 ppm to C3 (it is therefore referred to as C3' in Fig. 3e), leading to  $\bar{\delta}_{\text{C}}$  values of {154.5(C1), 150.8(C2), 148.0(C3)} ppm with relative intensities 1.00:1.44:1.01. The deviations from the expected exact 1:1:1 ratios (where the discrepancy is only significant for C2) mainly reflect that integrated  $^{13}\text{C}$  NMR-peak intensities obtained by  $^1\text{H} \rightarrow ^{13}\text{C}$  CPMAS NMR experiments do generally not exactly reproduce the corresponding  $^{13}\text{C}$  site



Table 1 NMR/DFT-derived  $^{13}\text{C}$  chemical shifts of  $\beta$ -caffeine<sup>a</sup>

Site	$\delta_{\text{C}}^j[\text{NMR}]$ (ppm)	$\bar{\delta}_{\text{C}}^j[\text{NMR}]$ (ppm)	$\bar{\delta}_{\text{C}}^j[\text{DFT}]$ (ppm)	$\delta_{\text{C}}^j[\text{DFT}]$ (ppm)				
C1	154.3	154.5 $\pm$ 0.2	153.0 $\pm$ 0.3	152.5	152.7	152.8	152.9	154.1
C2	151.2	150.8 $\pm$ 0.2	149.4 $\pm$ 0.3	148.3	148.9	149.5	149.7	150.5
C3 <sup>b</sup>	149.0/147.7	148.0 $\pm$ 0.2	147.5 $\pm$ 0.6	146.5	146.7	147.4	147.7	149.4
C4	142.8	143.5 $\pm$ 0.4	146.0 $\pm$ 1.3	142.9	143.9	145.0	148.9	149.3
C5	105.9	106.1 $\pm$ 0.2	107.8 $\pm$ 0.6	106.2	106.9	107.9	108.1	109.7
C6	35.4	35.0 $\pm$ 0.2	35.3 $\pm$ 0.6	33.7	34.8	35.4	35.7	36.7
C7 <sup>c</sup>	31.3/30.2	30.7 $\pm$ 0.2	29.6 $\pm$ 0.9	28.0	28.3	29.3	30.5	32.2
C8 <sup>c</sup>	30.2/28.5	29.6 $\pm$ 0.2	29.5 $\pm$ 0.6	27.7	28.6	29.2	29.9	32.0

<sup>a</sup>  $^{13}\text{C}$  chemical shift at the NMR peak maximum,  $\delta_{\text{C}}^j[\text{NMR}]$ , along with the center-of-gravity (average) chemical shift obtained by deconvolution of the MAS NMR spectrum (Fig. S3, ESI),  $\bar{\delta}_{\text{C}}^j[\text{NMR}]$ , or by DFT calculations,  $\bar{\delta}_{\text{C}}^j[\text{DFT}]$ ; the latter values are averages over the  $^{13}\text{C}$  chemical shift values of five distinct caffeine molecules in the unit cell, each of which is given in the five rightmost columns. <sup>b</sup> The C3 sites produces two resonances at 149.0 ppm and 147.7 ppm, which are labelled by “C3<sup>1</sup>” and “C3<sup>2</sup>” in Fig. 3e. <sup>c</sup> The “C78”  $^{13}\text{C}$  resonance intensity at 30.2 ppm (Fig. 3e) involves equal contributions from the  $^{13}\text{C}$ 7 and  $^{13}\text{C}$ 8 sites.

populations in the structure. Likewise, the  $^{13}\text{CH}_3$ -associated resonance at  $\delta_{\text{C}}^j = 30.2$  ppm, which is labelled “C78” in Fig. 3e, was deduced to involve equal contributions from  $^{13}\text{C}$ 7 and  $^{13}\text{C}$ 8. Upon distributing half of the NMR-signal intensity at  $\delta_{\text{C}}^j = 30.2$  ppm to each of  $^{13}\text{C}$ 7 ( $\delta_{\text{C}}^j = 31.3$  ppm) and  $^{13}\text{C}$ 8 ( $\delta_{\text{C}}^j = 28.5$  ppm), the as-obtained relative integrated NMR-signal intensities of the C6:C7:C8 sites become 1.00:1.03:0.96, which is in excellent agreement with the expected 1:1:1 ratios (Fig. S3, ESI†).

Further support for the spectral-deconvolution-derived attribution of the “C3<sup>1</sup>” and “C78” NMR peaks to the  $^{13}\text{C}$ 3 site and equal contributions to  $^{13}\text{C}$ 7/ $^{13}\text{C}$ 8, respectively, is provided by the resulting very close  $\{\delta_{\text{C}}^{j1}, \delta_{\text{C}}^{j2}, \delta_{\text{C}}^{j3}\} = \{148.0, 30.7, 29.6\}$  ppm values observed relative to the  $\{\delta_{\text{C}}^{j1}, \delta_{\text{C}}^{j2}, \delta_{\text{C}}^{j3}\} = \{147.8, 30.6, 29.0\}$  ppm counterparts of the structurally ordered  $\text{C}\cdot\text{H}_2\text{O}$  polymorph.<sup>22</sup> The excellent agreement between the average  $^{13}\text{C}$  chemical shifts (*i.e.*,  $\bar{\delta}_{\text{C}}^j$ ) of the disordered  $\beta$ -caffeine structure obtained by “down-projecting” its 10  $^{13}\text{C}$  NMR peaks to the unique 8  $^{13}\text{C}$  resonance-mapping of the  $\text{C}\cdot\text{H}_2\text{O}$  polymorph<sup>22</sup> is very gratifying. Moreover, almost all  $\delta_{\text{C}}^j/\bar{\delta}_{\text{C}}^j$  discrepancies between  $\beta$ -caffeine and  $\text{C}\cdot\text{H}_2\text{O}$  are well within the experimental uncertainties. For instance, the  $\{\delta_{\text{C}}^{j1}, \delta_{\text{C}}^{j2}, \delta_{\text{C}}^{j3}\}$  values of Table 1 agree within 0.2 ppm with the  $\{\delta_{\text{C}}^{j1}, \delta_{\text{C}}^{j2}, \delta_{\text{C}}^{j3}\}$  counterparts of  $\text{C}\cdot\text{H}_2\text{O}$ .<sup>22</sup> Significant chemical-shift differences between the two polymorphs are *only* observed for the  $^{13}\text{C}$ 2 and  $^{13}\text{C}$ 4 carbonyl sites, both of which are  $\approx 1.0$  ppm higher for  $\beta$ -caffeine than those of  $\text{C}\cdot\text{H}_2\text{O}$ , which is attributed to distinct HB scenarios between the two structures. DFT calculations (not shown) reveal that the crystallographically unique C4H site of  $\text{C}\cdot\text{H}_2\text{O}$  involves one  $\text{C4H}\cdots\text{OH}_2$  HB (201 pm), whereas the five distinct H4 sites of  $\beta$ -caffeine feature a range of HB distances to the O1 (198; 235; 250 pm), O2 (212 pm), and N (236 pm) sites of neighboring molecules. They contribute strongly to the “local” disorder of the  $^{13}\text{C}$ 4 environment, and thereby to its sizable fwhm value relative to any other  $^{13}\text{C}$ *j* site of  $\beta$ -caffeine, while also explaining the accompanying larger  $\delta_{\text{C}}^{j4}-\bar{\delta}_{\text{C}}^j$  difference (Table 1).

#### 4.3 NMR/GIPAW-derived $^{13}\text{C}$ chemical shifts of cocrystals and precursors

Fig. 4 contrasts the  $^{13}\text{C}$  CPMAS NMR spectra recorded from  $\beta$ -caffeine and its four cocrystals. The successful completion of each cocrystal reaction is evidenced both from our PXRD

analyses (Section 2.2) and by the unique  $^{13}\text{C}$ *j* site/chemical-shift mapping resulting for all cocrystals, for which  $\delta_{\text{C}}^j$  of each  $^{13}\text{C}_1\cdots^{13}\text{C}$ 22 site differs only slightly relative to that of its precursor phases (Table 2). In particular, each of the 8 caffeine-moiety-related  $^{13}\text{C}$  resonances is readily identified for each cocrystal, meaning that no cocrystal manifests NMR peaks traceable to either “C3<sup>1</sup>” or “C78” of Fig. 4e, thereby eliminating all NMR-peak assignment ambiguities of  $\beta$ -caffeine. Hence, all  $^{13}\text{C}$  resonance identifications for each cocrystal (Fig. 4) readily follow from those established for its parent phases (Fig. 3), as corroborated further by contrasting the experimental and DFT/GIPAW-generated  $\{\delta_{\text{C}}^j\}$  values listed in Table 2.

While hitherto no report on any *even partially complete* set of  $\{\delta_{\text{C}}^j\}$  data or  $^{13}\text{C}$  NMR-peak assignments appears to exist for the 2C-OA and C-ME cocrystals, very notable is the excellent agreement between the  $^{13}\text{C}$  chemical shifts obtained herein for 2C-MA and C-GA with those reported earlier by Vigilante and Mehta;<sup>50</sup> the truly marginal discrepancies of  $\leq 0.2$  ppm are well within the experimental uncertainties throughout, where systematic  $^{13}\text{C}$  MAS NMR shift-referencing errors often yield  $\delta_{\text{C}}^j$  discrepancies exceeding 0.5 ppm between studies. For instance, the two  $^{13}\text{C}$  chemical shifts reported by Bryce and coworkers for the  $^{13}\text{C}$ 4 (142.9 ppm)<sup>46</sup> and  $^{13}\text{C}$ 8 (28.3 ppm)<sup>49</sup> sites of C-ME accord with those of Table 2 within 0.3 ppm and 0.7 ppm, respectively.

Table 2 reveals a typical agreement of 2–3 ppm between the experimental and modeled  $\{\delta_{\text{C}}^j\}$  values across all diacid precursors and their corresponding cocrystals with caffeine, where deviations  $\leq 1$  ppm and  $\leq 3$  ppm result for 24 and 56 sites out of the entire ensemble of 68 sites/shifts, respectively. Out of the 12  $^{13}\text{C}$ *j* sites manifesting a  $> 3.0$  ppm  $\delta_{\text{C}}^j$  discrepancy between the model and experiment, however, 8 sites concern the GA and ME diacid precursors and their cocrystals, where the GIPAW calculations of the GA-associated phases consistently overestimate the  $^{13}\text{COOH}$  shifts, whereas the  $^{13}\text{CH}_2$  counterparts are in excellent agreement with experiments. That scenario is reversed for the ME/C-ME structures, for which the NMR/GIPAW-derived  $^{13}\text{COOH}$  chemical shifts accord well, whereas substantial deviations are observed for the  $^{13}\text{CH}$  sites (Table 2). Similar systematic errors—but of overall much smaller magnitudes—are observed for the 2C-OA and 2C-MA cocrystals and



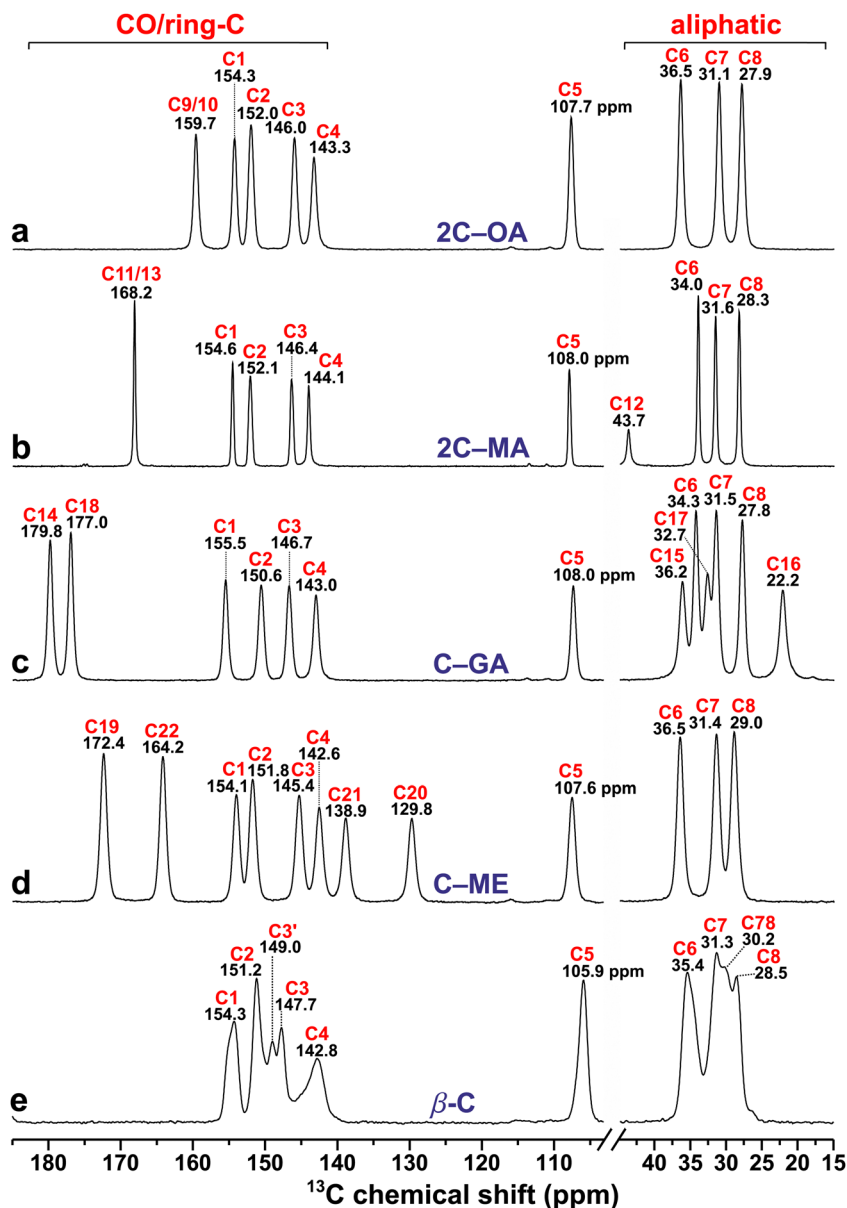


Fig. 4  $^{13}\text{C}$  CPMAS NMR spectra acquired at 14.1 T and 12.00 kHz MAS from cocrystals of  $\beta$ -caffeine and (a) oxalic acid (2C–OA), (b) malonic acid (2C–MA), (c) glutaric acid (C–GA), and (d) maleic acid (C–ME), along with the spectrum from (e)  $\beta$ -caffeine ( $\beta$ -C) for reference.

their OA, OA- $2\text{H}_2\text{O}$ , and MA precursors, where the modeled  $\{\delta_{\text{C}}^j\}$  values are consistently higher than their experimental counterparts. While Table 2 also reveals minor systematic discrepancies for the C1–C8 sites of the caffeine moiety in the cocrystals relative to  $\beta$ -caffeine, the GIPAW-derived  $\{\delta_{\text{C}}^j\}$  values are typically *lower* than those from NMR, except for C4/C5 that conform to the more typical trend of overestimated  $\delta_{\text{C}}$  values by the calculations.

Because most deviations between the NMR/GIPAW-derived  $^{13}\text{C}$  chemical shifts are *systematic*, they have little/no bearings on our analyses below that target the shift-difference between the cocrystals and precursors (Section 4.6). Nonetheless, the very significant discrepancies between a few experimental/modeled  $\delta_{\text{C}}$  values for the GA and ME moieties in both

precursor and cocrystal structures are reasons for concern. We remind that our  $\delta_{\text{C}}^j$  values of Table 2 originated from DFT energy minimizations where only the H positions were adjusted, except for  $\beta$ -caffeine, for which all unit-cell parameters and atom coordinates were optimized (Table S2, ESI<sup>†</sup>). That significantly improved the chemical-shift predictions, as reflected in a root-mean-square deviation (rmsd) of 1.4 ppm relative to the experimental shifts, which may be contrasted with the rmsd(DFT/NMR) = 2.0 ppm outcome that resulted by *only* adjusting the H atom positions of  $\beta$ -caffeine, or with the corresponding rmsd(DFT/NMR) = 3.0 ppm obtained across the entire  $\{\delta_{\text{C}}^j\}$  ensemble from all other phases (60 data points). Yet, there were no improvements by employing full-atom/cell optimizations of the {GA, C-GA} and {ME, C-ME} structures (which



Table 2 NMR/DFT-derived  $^{13}\text{C}$  chemical shifts of cocrystals and precursors<sup>a</sup>

Coformer	Site	Coformer $\delta_{\text{C}}$ (ppm)	2C-OA $\delta_{\text{C}}$ (ppm)	2C-MA $\delta_{\text{C}}$ (ppm)	C-GA $\delta_{\text{C}}$ (ppm)	C-ME $\delta_{\text{C}}$ (ppm)
$\beta$ -Caffeine <sup>b</sup>	C1	154.5(153.0)	154.3(153.1)	154.6(154.8)	155.5(154.5)	154.1(153.1)
	C2	150.8(149.4)	152.0(150.4)	152.1(150.1)	150.6(148.9)	151.8(150.5)
	C3	148.0(147.5)	146.0(147.0)	146.4(146.6)	146.7(148.5)	145.4(145.1)
	C4	143.5(146.0)	143.3(145.2)	144.1(146.6)	143.0(145.0)	142.6(143.2)
	C5	106.1(107.8)	107.7(110.9)	108.0(110.8)	107.4(110.6)	107.6(110.2)
	C6	35.0(35.3)	36.5(36.2)	34.0(33.0)	34.3(33.5)	36.5(36.6)
	C7	30.7(29.6)	31.1(28.5)	31.6(30.0)	31.5(29.1)	31.4(29.7)
	C8	29.6(29.5)	27.9(25.2)	28.3(25.8)	27.8(24.2)	29.0(27.4)
$\alpha$ -OA	C9/10	160.7(162.9)	159.7(162.2)			
$\alpha$ -OA·2H <sub>2</sub> O	C9/10	163.1(164.5)	159.7(162.2)			
$\beta$ -MA	C11	175.1(179.0)		168.2(170.1)		
	C12	40.8(39.7)		43.7(44.3)		
	C13	174.7(175.4)		168.2(170.1)		
$\beta$ -GA	C14	181.5(186.6)			179.8(183.4)	
	C15	33.8(33.8)			36.2(36.0)	
	C16	18.7(16.5)			22.2(22.0)	
	C17	33.8(33.8)			32.7(32.2)	
	C18	181.5(186.6)			177.0(182.8)	
I-ME	C19	172.9(173.4)				172.4(174.2)
	C20	133.1(141.4)				129.8(137.9)
	C21	140.1(148.1)				138.9(146.4)
	C22	169.2(168.5)				164.2(167.2)

<sup>a</sup>  $^{13}\text{C}$  chemical shifts ( $\delta_{\text{C}}^i$ ) for the  $^{13}\text{C}_j$  site labels of Fig. 1, obtained either experimentally from the shift at the NMR-peak maximum, or by DFT/GIPAW calculations (values within parentheses). The  $\delta_{\text{C}}$  uncertainties are around  $\pm 0.30$  ppm (DFT/GIPAW) and  $\pm 0.15$  ppm (NMR), except for  $\beta$ -caffeine (Table 1). <sup>b</sup> For  $\beta$ -caffeine (only), center-of-gravity  $^{13}\text{C}$  chemical shifts ( $\bar{\delta}_{\text{C}}$ ) are reported rather than  $\delta_{\text{C}}^i$ . The experimental  $\{\bar{\delta}_{\text{C}}\}$  data were obtained by deconvolution of the MAS NMR spectrum, while each DFT/GIPAW-derived  $\bar{\delta}_{\text{C}}$  value is the average chemical shift over five crystallographically distinct sites/molecules (see Table 1).

manifest the globally largest  $\delta_{\text{C}}^i$  discrepancies), whose  $\{\delta_{\text{C}}^i\}$  sets revealed an even larger  $\text{rmsd}(\text{DFT}/\text{NMR}) = 6.5$  ppm relative to its experimental counterpart, which exceeded that of  $\text{rmsd}(\text{DFT}/\text{NMR}) = 4.5$  ppm resulting by solely optimizing the H atom positions (Table 2). We have no satisfactory explanation for the large discrepancies ( $\gtrsim 5$  ppm) between the models and experiments for a few  $^{13}\text{C}$  sites of the GA/ME-related structures, which must originate from unaccounted structural effects.

#### 4.4. Factors governing the $^{13}\text{C}$ resonance widths

Here we discuss three factors expected to primarily govern the full width at half maximum (fwhm) height of the  $^{13}\text{C}$  signals observed from the cocrystals and their precursors (Table S4, ESI<sup>†</sup>), leading to some recommendations about the choice of external magnetic field ( $B_0$ ) for arranging (sub)optimal  $^{13}\text{C}$  MAS NMR spectral resolution. The two primary spectral-resolution-limiting factors involve so-called “inhomogeneous broadening”,<sup>61</sup> i.e.,  $^{13}\text{C}$  chemical-shift dispersions from either the anisotropic bulk magnetic susceptibility (ABMS)<sup>24,71–74</sup> or static structural disorder.<sup>18,20,21</sup> Both scale linearly with  $B_0$  on a frequency scale (in Hz), which complicates their discrimination if only having a  $^{13}\text{C}$  (CP)MAS NMR spectrum available.<sup>24,73,74</sup> Yet, the ABMS-stemming broadening in ppm is shared among all nuclear sites in the structure, regardless of their nuclide type or structural origin, meaning that the ABMS remains constant for all  $\{^{13}\text{C}_j\}$  and  $\{^1\text{H}_j\}$  sites in the sample,<sup>24,71–74</sup> in contrast to the local structural disorder that varies among

crystallographically distinct  $^{13}\text{C}_j$  sites, and thereby giving variable  $^{13}\text{C}$  fwhm values (in ppm). Hence, contrasting the (lack of) variations within the  $\{^{13}\text{C}_j\}$  fwhm set listed in Table S4 (ESI<sup>†</sup>) within each precursor/cocrystal helps gauging the potential presence of structural disorder.

Fig. 3 reveals that the  $^{13}\text{C}$  resonance widths vary markedly among the various well-ordered cocrystal precursors, which most likely reflects variable ABMS effects. The polycrystalline MA powder produces fwhm values of  $< 30$  Hz ( $\leq 0.2$  ppm at 14.1 T; Table S4, ESI<sup>†</sup>), which are typical for organic molecules in well-ordered crystals with negligible ABMS broadening. In contrast, the OA, OA·2H<sub>2</sub>O, and GA powders reveal 3–4 times broader  $^{13}\text{C}$  resonances than MA, whereas the  $^{13}\text{C}$  sites of the ME and  $\beta$ -caffeine specimens manifest substantially larger fwhm values of  $\approx 240$  Hz ( $\approx 1.6$  ppm) and 200–435 Hz (1.3–2.9 ppm), respectively. Here, the near-constant peakwidths observed for ME suggests that ABMS broadening mainly limits its  $^{13}\text{C}$  NMR spectral resolution, whereas structural disorder is mainly degrading that for  $\beta$ -caffeine, notably so in the CH<sub>3</sub> region (Fig. 3e). Indeed, the markedly larger  $^{13}\text{C}_j$  fwhm values of  $\beta$ -caffeine relative to all other specimens (Fig. 3 and 4) primarily stems from a significant (static) structural disorder,<sup>22,24</sup> where the lowest fwhm value of 1.3 ppm observed for the  $^{13}\text{C}_5$  resonance sets an upper limit of the ABMS contribution to all peak widths.

Despite the larger supramolecular aggregate of the cocrystal units, their  $^{13}\text{C}$  peak widths remain consistently narrower than



those of  $\beta$ -caffeine (Table S4, ESI<sup>†</sup>), which reflects a higher degree of local structural order of each cocrystal.<sup>12,14,24</sup> The relative  $^{13}\text{C}$  fwhm values increase along the series 2C-MA < 2C-OA < C-GA  $\lesssim$  C-ME, roughly following those of each respective pristine diacids (Table S4, ESI<sup>†</sup>) but with 1.2–6 times wider  $^{13}\text{C}$  resonances. Only the peakwidths from C-ME break that trend, where *narrower* peaks are observed relative to both the ME and  $\beta$ -caffeine crystallites for which ABMS and structural disorder primarily govern the respective  $^{13}\text{C}$  fwhm values, both apparently being reduced in the C-ME crystallites.

A third factor known to broaden  $^{13}\text{C}$  resonances from molecules featuring direct C–N bonds is the spin-1  $^{14}\text{N}$  nuclide (99.6% natural abundance) that may induce additional NMR-peak splittings/broadenings of nearby  $^{13}\text{C}$  sites by  $^{14}\text{N}$ – $^{13}\text{C}$  dipolar interactions, whose effects are incompletely suppressed by MAS and scale as  $B_0^{-1}$  (in Hz) and  $B_0^{-2}$  (in ppm).<sup>75,76</sup> Indeed, while demonstrated to vastly dominate the  $^{13}\text{C}$  MAS NMR-peak widths and the spectral resolution from C–H<sub>2</sub>O at a low magnetic field of 4.7 T but being negligible at  $B_0 = 21$  T,<sup>22</sup> we expect marginal signal broadenings for our experimentation at  $B_0 = 14.1$  T, as was also concluded in ref. 50. The data of Table S4 (ESI<sup>†</sup>) confirm those expectations, suggesting a  $<30$  Hz  $^{13}\text{C}$  resonance broadening from the  $^{14}\text{N}$ – $^{13}\text{C}$  dipolar interactions, as is also supported by the  $^{13}\text{C}$  NMR peak-width analysis of ref. 24 performed at  $B_0 = 11.7$  T, at which one expects slightly larger effects from  $^{14}\text{N}$ – $^{13}\text{C}$  interactions. From the marginal dipolar broadening to the net  $^{13}\text{C}$  fwhm values, we conclude that inhomogeneous ABMS and structural-disorder stemming  $^{13}\text{C}$  chemical-shift distributions dominate the NMR peak-widths throughout all specimens considered herein, as also suggested by our  $^1\text{H}$  NMR results (Section 4.5).

At least for anhydrous  $\beta$ -caffeine, however,  $^{13}\text{C}$  NMR experimentation at  $B_0 \geq 14.1$  T is advantageous for achieving sufficient resolution. Recalling the two additional C3' and C78 NMR peaks (Section 4.2) of anhydrous  $\beta$ -caffeine relative to its  $\alpha$  counterpart,<sup>22</sup> a puzzling feature is their apparent absence in several  $^{13}\text{C}$  MAS NMR spectra reported from  $\beta$ -caffeine in the literature,<sup>14,23,24</sup> incidentally rendering those spectra closer to that observed from  $\alpha$ -caffeine,<sup>22</sup> encompassing some results from “anhydrous caffeine” of unspecified phase identity.<sup>68,70</sup> Yet all those NMR spectra were recorded at *lower* magnetic fields of either 9.4 T (ref. 14 and 23) or 11.7 T (ref. 24) relative to those acquired at 14.1 T herein (Fig. 4e) and in ref. 12 along with the high-field result by Enright *et al.*<sup>22</sup> at  $B_0 = 21$  T. Evidently, *only* MAS NMR spectra recorded at  $B_0 \geq 14.1$  T give discernible  $^{13}\text{C}$  resonances at  $\approx 30$  ppm (C78) and  $\approx 149$  ppm (C3'), whereas those signals apparently coalesce with those from  $^{13}\text{C}7$ / $^{13}\text{C}8$  and  $^{13}\text{C}3$ , respectively, in NMR spectra obtained at  $B_0 < 14.1$  T.<sup>14,23,24</sup> This effect must stem from the resolution-degradation associated with lower- $B_0$  experimentation alone and/or its accompanying emphasized  $^{13}\text{C}$  resonance broadening from  $^{14}\text{N}$ – $^{13}\text{C}$  interactions. Likewise, the  $^{13}\text{C}$  MAS NMR spectrum obtained from “anhydrous caffeine” at 9.4 T by Nonappa and Kolehmainen<sup>68</sup> appears very similar to those reported from  $\beta$ -caffeine in ref. 14, 23 and 24.

We conclude that “high-field” NMR experimentation is beneficial for enabling complete  $^{13}\text{C}$  site/NMR-peak assignments of anhydrous  $\beta$ -caffeine, where  $B_0 = 14.1$  T appears to be the minimum magnetic field admitting resonance-discrimination between all crystallographically inequivalent  $^{13}\text{C}$  sites, potentially enabling  $^{13}\text{C}$  NMR quantifications of the  $\alpha$ / $\beta$ -caffeine contributions in a powder mixture without resorting to PXRD.

#### 4.5. $^1\text{H}$ NMR and DFT/GIPAW results

**4.5.1.  $^1\text{H}$  MAS NMR spectra.** Fig. 5 and 6 present the  $^1\text{H}$  NMR spectra from the precursors and cocrystals, respectively, all recorded at  $B_0 = 14.1$  T and fast MAS (60.0 kHz) to suppress the *normally* spectral-resolution-limiting homonuclear  $^1\text{H}$ – $^1\text{H}$  dipolar interactions.<sup>15–18</sup> Indeed, the relative

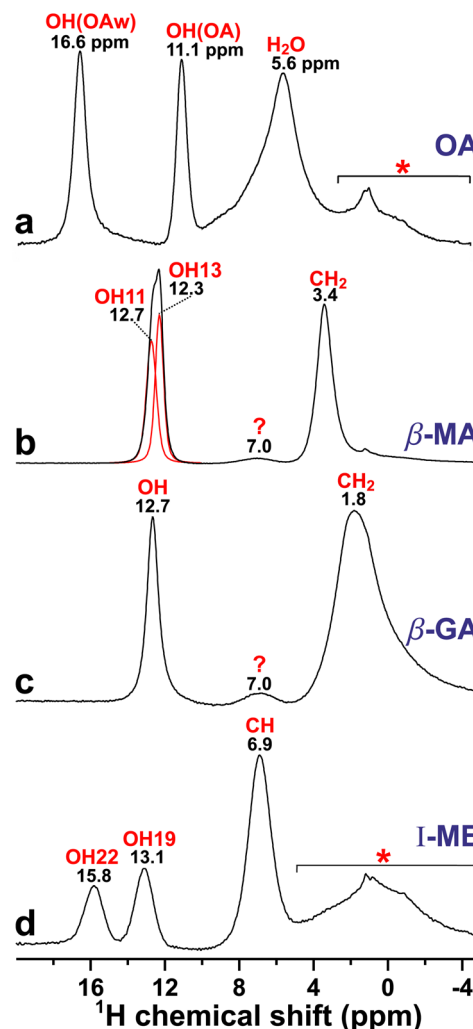
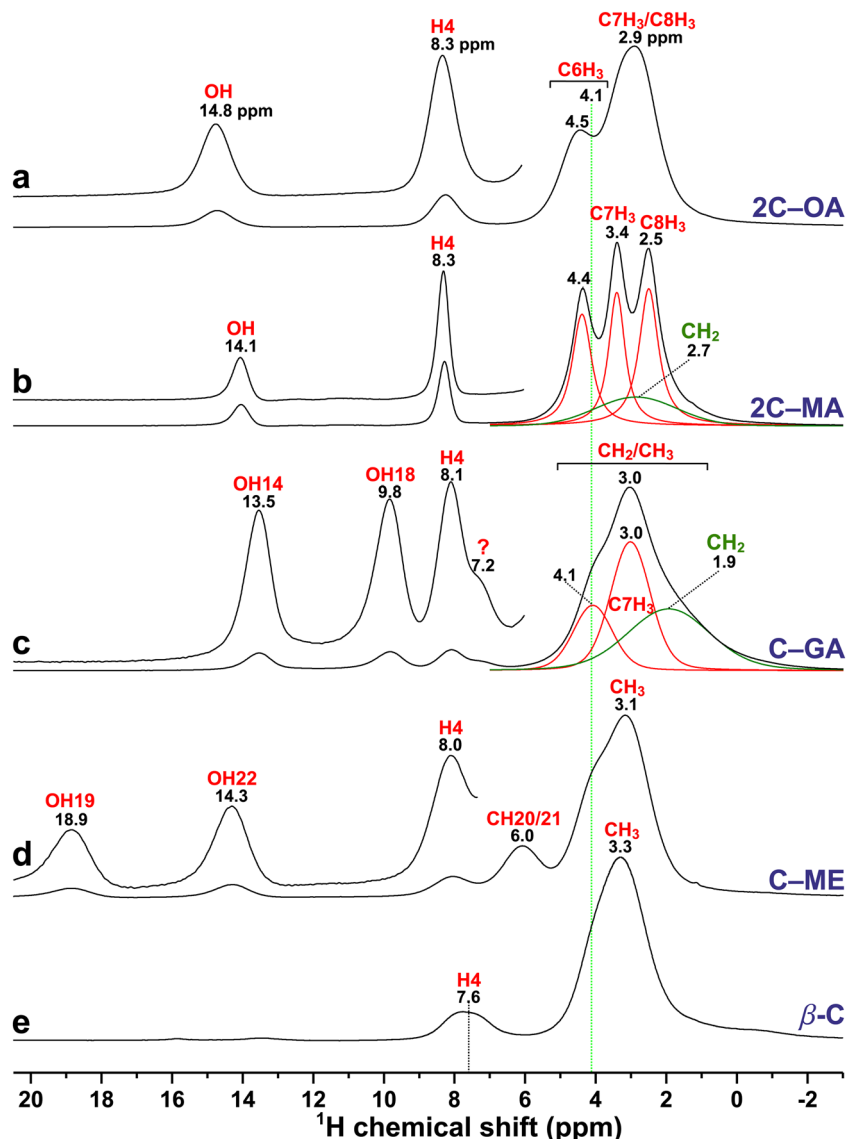


Fig. 5  $^1\text{H}$  MAS NMR spectra recorded at 14.1 T and 60.0 kHz MAS from the (a)  $\alpha$ -OA (“OA”) and  $\alpha$ -OA- $2\text{H}_2\text{O}$  (“OAw”) mixture together with powders from the other (b)  $\beta$ -MA, (c)  $\beta$ -GA, and (d) I-ME diacids. The red traces in (b) are deconvolution results of the two overlapping OH11/ OH13 resonances. The low-ppm resonance region marked by an asterisk in (a) and (d) reveal background signals from the NMR probehead, and the peak marked by “?” in (b) and (c) stems from an unknown impurity phase of the MA and GA precursors.





**Fig. 6**  $^1\text{H}$  MAS NMR spectra recorded at 14.1 T and 60.0 kHz MAS from the (a) 2C-OA, (b) 2C-MA, (c) C-GA, (d) C-ME cocrystals, and (e) anhydrous  $\beta$ -caffeine. The insets show vertically expanded zooms across the high-ppm spectral region. The red/green traces in (b) and (c) are deconvolution results of the overlapping  $\text{C}^1\text{H}_3$  (red) and  $\text{C}^1\text{H}_2$  (green) NMR signals. The vertical dotted line at  $\delta_{\text{H}} = 4.1$  ppm marks the approximate chemical shift of the  $\text{C}^1\text{H}_3$  resonance of the caffeine molecule for the C-GA, C-ME, and  $\beta$ -caffeine specimens in (c)–(e), which differ slightly from those of 2C-OA and 2C-MA in (a) and (b). The NMR peak marked by "?" in (c) stems from an unknown impurity of the GA precursor (see Fig. 5c).

$^1\text{H}$  NMR peak widths of the cocrystals match well those of the respective  $^{13}\text{C}$  NMR spectra (Fig. 4), further underscoring that the  $^1\text{H}/^{13}\text{C}$  resonance widths are governed primarily by chemical-shift dispersions stemming from variable ABMS<sup>24,71–74</sup> and structural disorder<sup>18,20,21</sup> effects among the specimens (Section 4.4). In the least ordered structure—*i.e.*, that of  $\beta$ -caffeine—all  $\text{C}^1\text{H}_3$ -stemming  $^1\text{H}$  resonances coalesce into a near-Gaussian peak, whereas the  $\text{C}^1\text{H}_3$  peak is discernible in all NMR spectra from the cocrystals (Fig. 6), *despite* a further overlap from  $\text{C}^1\text{H}_2$  signals in those from 2C-MA and C-GA. All three  $^1\text{H}_6$ – $^1\text{H}_8$  resonances are resolved from the most ordered cocrystal structure, *i.e.*, 2C-MA (Fig. 6b). Notably, the present  $^1\text{H}$  MAS NMR spectrum from  $\beta$ -caffeine is very similar to those of ref. 23 and 24 where the value of  $\delta_{\text{H}}^4 = 7.6$  ppm

reported by Bordignon *et al.*<sup>23</sup> is identical to ours (Table 3), despite that all  $\text{C}^1\text{H}_3$  resonances coalesced fully<sup>23,24</sup> (although, for unclear reasons, ref. 23 tabulated distinct  $^1\text{H}_6$  and  $^1\text{H}_7$ / $^1\text{H}_8$  shifts).

Nonetheless, the reduced  $^1\text{H}$  NMR spectral resolution in the aliphatic region, for which broadening from residual  $^1\text{H}$ – $^1\text{H}$  interactions is most pronounced, compromises accurate site-specific assessments of the  $^1\text{H}$  chemical-shift alterations upon cocrystal formation. Table 3 collects the NMR and DFT/GIPAW derived  $^1\text{H}$  chemical shifts, which constitute  $\delta_{\text{H}}^i$  data for all well-resolved signals but CG shifts ( $\delta_{\text{H}}^j$ ) for all heavily overlapping resonances. Hence, in what follows, we focus on the  $^1\text{H}_j$  resonances that are well resolved in the NMR spectra from *both* the precursors (Fig. 5) and their corresponding cocrystals

Table 3 NMR/DFT-derived  $^1\text{H}$  chemical shifts of cocrystals and precursors<sup>a</sup>

Coformer	Site	Coformer $\delta_{\text{H}}/\text{ppm}$	2C-OA $\delta_{\text{H}}/\text{ppm}$	2C-MA $\delta_{\text{H}}/\text{ppm}$	C-GA $\delta_{\text{H}}/\text{ppm}$	C-ME $\delta_{\text{H}}/\text{ppm}$
$\beta$ -Caffeine <sup>b</sup>	H4	7.6(8.4)	8.3(7.2)	8.3(7.6)	8.1(7.3)	8.0(6.7)
	H6/7/8 <sup>c</sup>	3.3(3.8)	3.3(2.6)	3.4(2.8)	3.3(2.7)	3.4(2.6)
$\alpha$ -OA $\alpha$ -OA·2H <sub>2</sub> O	HO9/10	11.1(11.2)	14.8(15.0)			
	HO9/10	16.6(17.8)	14.8(15.0)			
	H <sub>2</sub> O	5.6(5.6)				
$\beta$ -MA	HO11	12.7(13.7)		14.1(14.8)		
	H12a/b	3.4(2.6)		2.7(1.7)		
	HO13	12.3(13.4)		14.1(14.8)		
$\beta$ -GA	HO14	12.7(13.7)			13.5(14.0)	
	H15/16/17	1.8(1.2)			1.9(1.0)	
	HO18	12.7(13.7)			9.8(10.6)	
I-ME	HO19	13.1(13.6)				18.9(20.2)
	H20/21	6.9(6.2)				6.0(4.9)
	HO22	15.8(16.2)				14.3(14.6)

<sup>a</sup>  $^1\text{H}$  chemical shifts ( $\delta_{\text{H}}^i$ ) for the C<sub>j</sub> $^1\text{H}$  site labels of Fig. 1, obtained either experimentally from the shift at the NMR-peak maximum, or by DFT/GIPAW calculations (values within parentheses). The  $\delta_{\text{H}}$  uncertainties are around  $\pm 0.30$  ppm (GIPAW) and around  $\pm 0.15$  ppm for the experimental values for all well-resolved NMR peaks ( $\pm 0.5$  ppm for those obtained by spectral deconvolution; Fig. 6). <sup>b</sup> All GIPAW-derived shifts for  $\beta$ -caffeine are averages of the five  $\{\delta_{\text{H}}^i\}$  values of the inequivalent molecules in the unit cell. <sup>c</sup> Owing to the complete overlap among the C<sub>6</sub>H<sub>3</sub>, C<sub>7</sub>H<sub>3</sub>, and C<sub>8</sub>H<sub>3</sub> resonances in  $\beta$ -caffeine, only the average chemical-shift values are reported. However, the NMR spectra from the cocrystals admitted further site/signal-resolution by spectral deconvolution, yielding the following NMR-derived  $\delta_{\text{H}}^i$  (or average CG  $\bar{\delta}_{\text{H}}$  chemical shifts), with the corresponding GIPAW-derived data given within parentheses: for 2C-OA,  $\delta_{\text{H}}^6 = 4.5$  (3.7) ppm;  $\bar{\delta}_{\text{H}}^{7/8} = 2.9$  (2.1) ppm; for 2C-MA,  $\delta_{\text{H}}^6 = 4.4$  (3.8) ppm;  $\delta_{\text{H}}^7 = 3.4$  (2.8) ppm;  $\delta_{\text{H}}^8 = 2.5$  (1.8) ppm; for C-GA,  $\delta_{\text{H}}^6 = 4.1$  (3.5) ppm;  $\bar{\delta}_{\text{H}}^7 = 3.0$  (2.3) ppm; for C-ME,  $\delta_{\text{H}}^6 = 4.1$  (3.2) ppm;  $\bar{\delta}_{\text{H}}^7 = 3.1$  (2.3) ppm.

(Fig. 6), namely COO $^1\text{H}$  of the diacid molecules, C4 $^1\text{H}$  of caffeine, and the equivalent C $^1\text{H}$ 20/21 sites of ME.

**4.5.2.  $^1\text{H}$  chemical shifts of carboxy groups.** Here, we discuss the set  $\{\delta_{\text{H}}^i\}$  of COO $^1\text{H}$  chemical shifts, assessed directly from the respective NMR-peak maximum shift values of Fig. 5 and 6 and assigned such that the highest/lowest chemical shift represents the H<sub>j</sub> site with shortest/longest H···O distance in the diacid/cocrystal structure. These  $^1\text{H}_j/\delta_{\text{H}}^i$  assignments are further corroborated by the DFT/GIPAW calculations (Table 3). The herein observed COO $^1\text{H}$  chemical shifts from the  $\alpha$ -OA·2H<sub>2</sub>O,  $\beta$ -MA, and ME powders agree within 0.3 ppm with the  $\delta_{\text{H}}^i$  values reported by Harris *et al.*<sup>34</sup> by using CRAMPS (combined rotation and multiple-pulse spectroscopy) to suppress NMR-peak broadenings from  $^1\text{H}$ – $^1\text{H}$  interactions under slow-MAS conditions. This excellent agreement is well within the experimental uncertainties, while moreover  $\delta_{\text{H}}^9$  of  $\alpha$ -OA·2H<sub>2</sub>O (16.6 ppm) matches perfectly that reported earlier by Berglund and Vaughan<sup>77</sup> (16.5 ppm). Notably, the chemical shifts observed by us from MA and ME agree much better with those of Harris *et al.*<sup>34</sup> than with ref. 77 but the former study did not include  $\alpha$ -OA. Although the experimental shift  $\delta_{\text{H}}^{9/10} = 11.1$  ppm (Table 3) is reproduced within 0.1 ppm by our GIPAW calculations, there is a significant deviation with that of 12.6 ppm reported in ref. 77 which is well outside of our experimental uncertainties. We believe that the herein reported  $\delta_{\text{H}}^{9/10} = 11.1$  ppm value of  $\alpha$ -OA is the hitherto most accurate result.

The COO $^1\text{H}$  chemical shifts of the pristine diacids presented in Fig. 5 correlate qualitatively well with the H···O distances of their crystal structures (Fig. 2): the two  $\alpha$ -OA·2H<sub>2</sub>O and  $\alpha$ -OA structures reveal the highest (16.6 ppm) and lowest (11.1 ppm) chemical shifts, respectively, as expected from their

corresponding shortest (146 pm) and longest (175 pm) HB lengths among all diacids (see caveat below). All COO $^1\text{H}$  sites of MA and GA along with H19 of ME feature essentially identical H-bond distances of 162–165 ppm (Fig. 2), as is mirrored in very similar  $\delta_{\text{H}}^i$  values between 12.3–13.1 ppm (Fig. 5). Notably, the  $^1\text{H}$  NMR signals from the two crystallographically inequivalent OH11 and OH13 sites of MA are discernible in Fig. 5b, despite their very small chemical-shift separation of 0.4 ppm stemming from a minute H···O bond-length difference of 1 pm (Fig. 2d), as also reproduced near-perfectly by the GIPAW calculations (0.3 ppm shift-difference).

Within a consistent but minor overestimation of the DFT/GIPAW-derived  $^1\text{H}$  chemical shift within typically  $\lesssim 1$  ppm (Table 3), the calculated  $\{\delta_{\text{H}}^i\}$  values match the experimental counterparts very well for all COO $^1\text{H}$  sites. Note that while all diacid structures feature H···O bonds, all cocrystals involve H···N contacts with the “N” atom of caffeine, except for the OH18···O14 bond in C-GA and OH22···O19 in C-ME (Fig. 2). Each NMR/GIPAW-derived  $\{\delta_{\text{H}}^i\}$  dataset gave a good linear correlation with the shortest H···O or H···N distance, denoted  $r(\text{H}\cdots\text{O}/\text{N})$ , throughout all COO $^1\text{H}$  sites. Fig. 7 plots the experimental and calculated  $^1\text{H}$  chemical shifts along with the corresponding best-fit results given by

$$\delta_{\text{H}}^i[\text{NMR}]/\text{ppm} = 47.0 - 0.208r(\text{H}\cdots\text{O}/\text{N})/\text{pm} \quad (R^2 = 0.912), \quad (3)$$

$$\delta_{\text{H}}^i[\text{DFT}]/\text{ppm} = 50.0 - 0.222r(\text{H}\cdots\text{O}/\text{N})/\text{pm} \quad (R^2 = 0.919), \quad (4)$$

both of which verify the expected trend<sup>34,35,39,40,42</sup> of an increasing  $^1\text{H}$  chemical shift for decreasing HB length. Indeed, both the



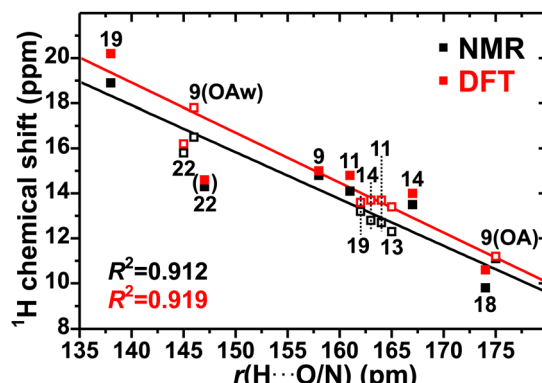


Fig. 7 Experimental (black symbols) and DFT/GIPAW-generated (red)  $^1\text{H}$  chemical shifts of the carboxy moieties of the pristine diacids (solid symbols) and the cocrystals (open) plotted against the  $\text{H}\cdots\text{O}/\text{H}\cdots\text{N}$  distance,  $r(\text{H}\cdots\text{O}/\text{N})$ , given in Fig. 2. The number around each data-point represents the proton label of Fig. 1. The lines are best-fit results, eqn (3) and (4), obtained by omitting one outlier data point ( $\delta_{\text{H}}^{22}$ ) and yielding the as-indicated  $R^2$  correlation coefficients. All chemical-shift uncertainties are within the symbol sizes.

experimental and modeled  $\{\delta_{\text{H}}^j\}$  sets are captured well by their very similar best-fit expressions and nearly equal correlation coefficients. Only the H22 site of ME breaks the trend, manifesting lower experimental and calculated shifts than those predicted from the very short intramolecular  $\text{H}\cdots\text{O}$  distance of 145 pm within the diacid unit (*vide supra*).

**4.5.3 COO<sup>1</sup>H chemical-shift changes upon cocrystal formation.** To monitor the  $^1\text{H}$  chemical-shift alterations upon cocrystal formation, we define the *difference* between the chemical shift of site  $^1\text{H}^j$  in the cocrystal,  $\delta_{\text{H}}^j[\text{C-X}]$ , relative to that in each pristine coformer,  $\delta_{\text{H}}^j[\text{X}]$ , where X represents  $\beta$ -caffeine or one of the {OA, OA·H<sub>2</sub>O, MA, GA, ME} diacids,

$$\Delta_{\text{H}}^j = \delta_{\text{H}}^j[\text{C-X}] - \delta_{\text{H}}^j[\text{X}], \quad \text{with } 1 \leq j \leq 22, \quad (5)$$

Table 4  $^1\text{H}$  Chemical-shift differences between cocrystals and precursors<sup>a</sup>

Coformer	Site	2C-OA $\Delta_{\text{H}}^j/\text{ppm}$	2C-MA $\Delta_{\text{H}}^j/\text{ppm}$	C-GA $\Delta_{\text{H}}^j/\text{ppm}$	C-ME $\Delta_{\text{H}}^j/\text{ppm}$
$\beta$ -Caffeine	H4 H6/7/8 <sup>b</sup>	0.6(-1.2) 0.0(-1.2)	0.7(-0.8) 0.1(-1.0)	0.5(-1.1) 0.0(-1.1)	0.4(-1.7) 0.1(-1.2)
$\alpha$ -OA $\alpha$ -OA·2H <sub>2</sub> O	HO9/10 HO9/10	3.8(3.8) -1.8(-2.8)			
$\beta$ -MA	HO11 H12a/b HO13		1.3(1.1) -0.7(-0.9) 1.8(1.4)		
$\beta$ -GA	HO14 H15/16/17 HO18			0.8(0.3) 0.1(-0.2) -2.9(-3.1)	
I-ME	HO19 H20/21 HO22				5.8(6.6) -0.9(-1.3) -1.5(-1.6)

<sup>a</sup> Chemical-shift differences ( $\Delta_{\text{H}}^j$ ) defined by eqn (5) and calculated from  $\delta_{\text{H}}^j$  data with two decimals. <sup>b</sup> Average chemical-shift values over all C6H<sub>3</sub>, C7H<sub>3</sub>, and C8H<sub>3</sub> sites of the caffeine moiety; see Table 3.

and the index  $j$  runs over all proton-bearing  $\text{C}_j$  sites of Fig. 1. The linear  $\delta_{\text{H}}^j/r(\text{H}\cdots\text{O}/\text{N})$  trends of Fig. 7 readily rationalize the observed COO<sup>1</sup>H chemical-shift alterations, whose values are presented in Table 4 along with those for the other C<sup>1</sup>H<sub>n</sub> sites (the latter are discussed in Section S1). Fig. S4 (ESI<sup>†</sup>) plots the NMR/DFT-derived  $\Delta_{\text{H}}^j$  values against the *difference* between the shortest  $\text{H}\cdots\text{O}/\text{N}$  distance of each cocrystal and precursor, which is denoted by  $\Delta r(\text{H}\cdots\text{O}/\text{N})$ .

For the COO<sup>1</sup>H chemical-shift changes ( $\Delta_{\text{H}}^j$ ), Table 4 reveals an overall trend of *higher*  $\delta_{\text{H}}^j$  values of the cocrystals (*i.e.*,  $\Delta_{\text{H}}^j > 0$ ), as is witnessed by Fig. 7 and rationalized from the typically *shorter*  $\text{H}\cdots\text{O}$  distance encountered in the cocrystal relative to that of the pristine diacid (Fig. 2). Such HB-length effects also account for the higher  $\delta_{\text{H}}^9$  value of 2C-OA relative to its  $\alpha$ -OA counterpart, as well as for the increased  $\delta_{\text{H}}^{11}$  and  $\delta_{\text{H}}^{13}$  values upon 2C-MA cocrystal formation. Likewise, the lower  $\delta_{\text{H}}^9$  value of 2C-OA relative to  $\alpha$ -OA·2H<sub>2</sub>O—along with the lower chemical shift of  $^1\text{H}^{18}$  of C-GA compared to the identical values  $\delta_{\text{H}}^{14} = \delta_{\text{H}}^{18}$  of the crystallographically equivalent COO<sup>1</sup>H sites of  $\beta$ -GA—are readily understood from the longer  $\text{H}\cdots\text{O}$  distances in the cocrystals.

#### 4.6. $^{13}\text{C}$ chemical-shift changes upon cocrystal formation

In direct analogy with the  $^1\text{H}$  chemical-shift difference between the cocrystal and its precursors [eqn (5)], we define

$$\Delta_{\text{C}}^j = \delta_{\text{C}}^j[\text{C-X}] - \delta_{\text{C}}^j[\text{X}], \quad \text{with } 1 \leq j \leq 22, \quad \text{and} \\ \text{X} = \{\beta\text{-C, OA, OA}\cdot 2\text{H}_2\text{O, MA, GA, ME}\}, \quad (6)$$

as the corresponding  $\delta_{\text{C}}^j$  alteration when each {2C-OA, 2C-MA, C-GA, C-ME} cocrystal is formed. Table 5 compiles the  $\{\Delta_{\text{C}}^j\}$  data obtained either by NMR experiments or GIPAW calculations. However, as for the  $^1\text{H}$  chemical-shift/structure correlations (except those for COO<sup>1</sup>H), the  $\delta_{\text{C}}^j$  and  $\Delta_{\text{C}}^j$  data only admits qualitative discussions.

Table 5  $^{13}\text{C}$  Chemical-shift differences between cocrystals and precursors<sup>a</sup>

Coformer	Site	2C-OA $\Delta_C^j/\text{ppm}$	2C-MA $\Delta_C^j/\text{ppm}$	C-GA $\Delta_C^j/\text{ppm}$	C-ME $\Delta_C^j/\text{ppm}$
$\beta$ -Caffeine	C1	-0.2(0.1)	0.0(1.8)	1.0(1.5)	-0.5(0.1)
	C2	1.2(1.0)	1.3(0.7)	-0.2(-0.5)	1.0(1.1)
	C3	-2.0(-0.6)	-1.6(-0.9)	-1.3(1.0)	-2.7(-2.4)
	C4	-0.1(-0.8)	0.6(0.6)	-0.4(-1.0)	-0.9(-2.8)
	C5	1.7(3.2)	1.9(3.1)	1.4(2.8)	1.5(2.5)
	C6	1.4(0.9)	-1.0(-2.3)	-0.7(-1.7)	1.5(1.4)
	C7	0.4(-1.1)	0.9(0.3)	0.8(-0.6)	0.7(0.0)
	C8	-1.7(-4.3)	-1.3(-3.7)	-1.8(-5.3)	-0.7(-2.0)
$\alpha$ -OA	C9/10	-1.1(-0.7)			
$\alpha$ -OA·2H <sub>2</sub> O	C9/10	-3.5(-2.3)			
$\beta$ -MA	C11		-6.9(-8.8)		
	C12		2.9(4.6)		
	C13		-6.5(-5.3)		
$\beta$ -GA	C14			-1.6(-3.3)	
	C15			2.4(2.2)	
	C16			3.4(5.5)	
	C17			-1.1(-1.6)	
	C18			-4.5(-3.9)	
I-ME	C19				-0.4(0.7)
	C20				-3.3(-3.5)
	C21				-1.1(-1.7)
	C22				-5.0(-1.3)

<sup>a</sup> Chemical-shift differences ( $\Delta_C^j$ ) defined by eqn (6) and calculated from  $\delta_C^j$  data with two decimals.

In contrast with the  $^{13}\text{CH}_2$  shifts of MA and GA, which deshield slightly by a few ppm, significantly decreased  $\delta_C$  values are observed for the  $^{13}\text{COOH}$  diacid sites, whose adjacent O atom form an HB with protons of neighboring caffeine/diacid molecules, which along with  $\text{COO}^- \rightarrow \text{COOH}$  conversions are well known to decrease the  $^{13}\text{C}$  shift in various molecular systems.<sup>37,38,78-81</sup> However, that trend has remained qualitative without any firm quantitative relationship having thus far been established between the *isotropic*  $^{13}\text{C}$  chemical shift and the  $^{13}\text{COH} \cdots \text{O}$  or  $^{13}\text{CO} \cdots \text{HO}$  distance (the principal value  $\delta_{yy}^j$  of the chemical-shift tensor, however, correlates linearly with the HB distance/angle parameters<sup>36-38</sup>). Indeed, the plot of  $\delta_C^j$  against  $r(\text{H} \cdots \text{O}/\text{N})$  in Fig. 8 reveals a significant scatter for the diacid/cocrystal structures. Although a weak trend of  $^{13}\text{COOH}$  shift-reduction with a shortened  $\text{COO} \cdots \text{H}$  distance is discernible, our data do not reveal any reasonable  $\delta_C^j/r(\text{H} \cdots \text{O}/\text{N})$  or  $\Delta_C^j/\Delta r(\text{H} \cdots \text{O}/\text{N})$  correlation for either the experimental or modeled data. The only exceptions are the  $^{13}\text{COOH}$  sites of the 2C-OA ( $\delta_C^9$ ), 2C-MA ( $\delta_C^{11}$ ), and C-GA ( $\delta_C^{14}$ ) cocrystals, all of which share the feature of a strong  $\text{H} \cdots \text{N}$  bond to the N atom of the caffeine molecule (which is expected to constitute the primary stabilization of the supramolecular structure<sup>8</sup>): they establish an excellent linear  $\delta_C^j/r(\text{H} \cdots \text{N})$  relationship (Fig. 8) for both the NMR and GIPAW-derived shifts but with the caveat that only three data points underlie the correlation.

Turning to the  $\delta_C^j$  changes of the caffeine moiety in the cocrystals relative to  $\beta$ -caffeine, Table 5 reveals the overall largest observed  $|\Delta_C^j|$  values for the {C3, C5, C8} sites upon cocrystal formation (and to a lesser extent, C2 and C6), thereby

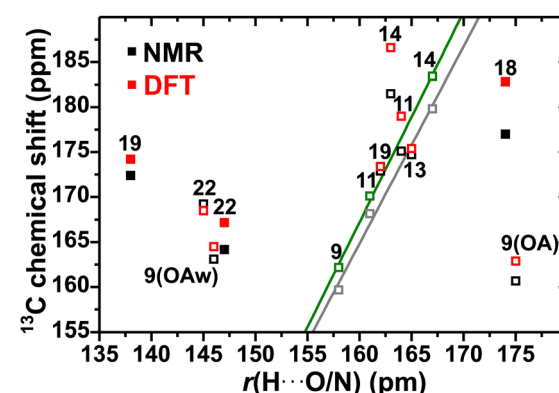


Fig. 8 Experimental (black symbols) and DFT/GIPAW-generated (red)  $^{13}\text{C}$  chemical shifts of the carboxy moieties of the pristine diacids (solid symbols) and the cocrystals (open) plotted against the  $\text{H} \cdots \text{O}$  or  $\text{H} \cdots \text{N}$  distance,  $r(\text{H} \cdots \text{O}/\text{N})$ , within each structure (Fig. 2). Each number represents the corresponding  $C_j$  label of Fig. 1. The symbols set in green and gray color for the NMR and DFT/GIPAW data, respectively, correspond to the results obtained from the 2C-OA ( $\delta_C^9$ ), 2C-MA ( $\delta_C^{11}$ ), and C-GA ( $\delta_C^{14}$ ) cocrystals, all of which are H-bonded to the "N" atom of caffeine. The corresponding lines are best-fit results to the expressions  $\delta_C^j[\text{NMR}]/\text{ppm} = -185.6 + 2.1905r(\text{H} \cdots \text{N})/\text{pm}$  ( $R^2 = 0.990$ ) and  $\delta_C^j[\text{DFT}]/\text{ppm} = -206.5 + 2.336r(\text{H} \cdots \text{N})/\text{pm}$  ( $R^2 = 0.998$ ), respectively. All chemical-shift uncertainties are within the symbol sizes.

suggesting that those local  $^{13}\text{C}$  electronic environments alter the most by the intermolecular caffeine-coformer interactions in the cocrystals structure (Fig. 2) relative to the caffeine-caffeine contacts in  $\beta$ -caffeine. The C3 and C5 atoms constitute



a C=C fragment between the pyriminedione and imidazolium rings (Fig. 1). We attribute the (globally largest) chemical-shift alteration of the C3 site of the caffeine molecule to its close proximity to the N atom, whose N···HOOC HB constitutes the primary intermolecular interaction in all cocrystal structures;<sup>8</sup> see Section 3 and Fig. 2. However, while the <sup>13</sup>C3 site *shields* upon cocrystal formation ( $\Delta_C^3 < 0$ ), <sup>13</sup>C5 *deshields* ( $\Delta_C^5 > 0$ ) to a comparable extent, for unknown reasons when considering its remoteness to any atom of a neighboring molecule in either the  $\beta$ -caffeine or cocrystal structures. The <sup>13</sup>CH<sub>3</sub> shift alterations are discussed in Section 4.7.

As commented in Section 4.5, the C4<sup>1</sup>H chemical shift remains near-constant throughout all cocrystals, which is attributed to  $\Delta_C^4$  cancellation-effects from variable and complex H-bonding scenarios. Likewise, only minor chemical-shift alterations are observed for <sup>13</sup>C4H, which besides being directly linked to the H-bonded “N” site of caffeine, *additionally* experiences weak H bonds to the CO atoms of the diacid carboxy groups upon cocrystal formation (Fig. 2). We speculate that the chemical-shift effects from those two competing H bonds might partially cancel each other. We remark that even slightly more negative  $\Delta_C^4$  values of {−1.3, −0.5, −1.6, −2.0} ppm apply if the respective {2C-OA, 2C-MA, C-GA, C-ME} cocrystals would be prepared from the ordered C-H<sub>2</sub>O phase that features  $\delta_C^4 = 144.6$  ppm<sup>22</sup> and one C4H···OH<sub>2</sub> bond.

#### 4.7 Tetrel-bonding effects on methyl <sup>13</sup>C/<sup>1</sup>H chemical shifts

Besides the possibility of a weak HB, the electrophilic nature of methyl groups offer the option of a H<sub>3</sub>C···O TB to a proximate electronegative and nucleophilic atom.<sup>47–49</sup> From our as-observed  $\Delta_H^i/\Delta_C^i$  data for the three <sup>13</sup>CH<sub>3</sub> groups of the caffeine moiety upon cocrystal formation, we discuss the complex HB/TB interplay on their <sup>13</sup>C/<sup>1</sup>H chemical shifts in relation to current literature, which is both sparse and inconclusive. Likewise, our data may only be discussed qualitatively.

Both DFT calculations<sup>48,49</sup> and NMR experiments<sup>49</sup> suggest consistently larger  $\delta_C$  than  $\delta_H$  alterations when a TB is formed. Scheiner *et al.*<sup>48</sup> investigated the <sup>13</sup>CH<sub>3</sub> and C<sup>1</sup>H<sub>3</sub> chemical-shift displacements upon CH···O HB or HC···O TB formation by DFT calculations, inferring that both <sup>1</sup>H and <sup>13</sup>C chemical shifts *increase* for either scenario, with the precise deshielding depending on the TB-length and N-C-O bond angle ( $\theta_{TB}$ ). The largest chemical-shift alterations occurred for a linear TB constellation, for which  $\Delta_C^i \leq 6$  ppm was predicted, whereas the <sup>1</sup>H chemical shift only increased marginally ( $\lesssim 1$  ppm).<sup>48</sup> Formation of a weak CH···O HB, however, is reported to produce a comparably larger <sup>1</sup>H deshielding than for <sup>13</sup>C.<sup>43,46,48</sup> Currently no firm/general experimental correlation is reported of either the <sup>1</sup>H or <sup>13</sup>C chemical shifts against the CH<sub>3</sub>···O or H<sub>3</sub>C···O distance. A recent compilation by Southern *et al.*<sup>49</sup> of experimental <sup>13</sup>C/<sup>1</sup>H chemical shifts from the literature along with GIPAW calculations, suggested very scattered <sup>13</sup>C/<sup>1</sup>H chemical-shift-structure correlations of CH<sub>3</sub> groups involved in tetrel bonds:<sup>49</sup> although experiments confirm that  $\delta_C^i$  is often increased for decreasing HC···O distance, no significant dependence was observed *versus*  $\theta_{TB}$ , nor of  $\delta_H^i$

against either the TB distance or  $\theta_{TB}$ . Moreover, when HB and TB bonds coexist for a CH<sub>3</sub> group, their effects on  $\delta_C^i$  may either reinforce or counteract each other.<sup>49</sup>

The <sup>13</sup>C and <sup>1</sup>H chemical-shift data from the current cocrystals accord qualitatively with previous findings of a smaller  $\delta_H^i$  than  $\delta_C^i$  change when the TB scenario alters between  $\beta$ -caffeine and its cocrystals. The NMR-derived value  $\Delta_H^{6/7/8} \approx 0$  apply throughout all cocrystals. Although the  $\delta_H^i$ /TB distance-accuracy is compromised by the lack of NMR-signal discrimination among the <sup>1</sup>H6–<sup>1</sup>H8 methyl resonances from  $\beta$ -caffeine, the near-constant <sup>1</sup>H chemical shift is also confirmed by the DFT calculations (within a constant shift-displacement of  $\Delta_H^{6/7/8} \approx -1$  ppm), for which each  $\delta_H^i$  and  $\Delta_H^i$  value is readily determined (Table S5, ESI†). Consistently larger <sup>13</sup>C chemical-shift displacements occur on cocrystal formation, where Table 2 reveals the largest changes for <sup>13</sup>C8H<sub>3</sub>, all of which are negative and conforming to the experimental range of  $-1.8 \leq \Delta_C^8/\text{ppm} \leq -1.3$ , whereas more negative values are predicted by the GIPAW calculations:  $-5.3 \leq |\Delta_C^8|/\text{ppm} \leq -2.0$ . Somewhat lower shift-differences (0.7–1.5 ppm) are observed for the <sup>13</sup>C6H<sub>3</sub> sites, where 2C-OA and C-ME yield *positive*  $\Delta_C^6$  values, while those for 2C-MA and C-GA are *negative* (Table 5). Besides slightly larger *magnitudes* predicted by the GIPAW calculations, all positive/negative  $\Delta_C^6$  trends are reproduced, as well as the experimental finding that <sup>13</sup>C7H<sub>3</sub> consistently manifests the smallest shift-change for each cocrystal.

Unfortunately, the  $\Delta_C^i$  trends identified above for the three <sup>13</sup>CH<sub>3</sub> sites of the caffeine moiety are for several reasons very difficult to rationalize: (i)  $\delta_C^i$  is expected to depend on both H···O/N and C···O/N distance-*changes* between  $\beta$ -caffeine and each cocrystal, whose effects on the chemical shift may augment or cancel partially. (ii) Even if *only* each *shortest* HB/TB distance per <sup>13</sup>CH<sub>3</sub> site of the cocrystal is considered (which is expected to be most influential on  $\delta_C^i$ ), the presence of five inequivalent molecules in the  $\beta$ -caffeine unit cell implies a complex reference scenario with a *range* of HB/TB lengths relative to the structurally ordered cocrystals. (iii) The current absence of any firm  $\delta_C^i/r(\text{CH}_n\cdots\text{O})$  or  $\delta_C^i/r(\text{CH}_n\cdots\text{O})$  correlation in conjunction with (i) and (ii), complicate the establishment of even semiquantitative  $\Delta_C^i$  correlations with the HB/TB-distance alterations accompanying the {2C-OA, 2C-MA, C-GA, C-ME} formation.

The shortest HB and TB distances of the methyl groups in  $\beta$ -caffeine and the cocrystals are compiled in Table S3 (ESI†). We first consider the most pronounced <sup>13</sup>C chemical-shift change upon cocrystal formation—*i.e.*,  $\Delta_C^8$ , assuming that the HB effects are minor because the range of C8H<sub>3</sub>···O1/O2 distances (236–294 pm) in  $\beta$ -caffeine span those of the cocrystals (and is thereby expected to give, on the average, a very similar  $\bar{\delta}_C^8$  contribution as for the cocrystals). Hence, the corresponding TB-length alterations are expected to primarily govern  $\Delta_C^8$ . Notably, the TB distances are overall shorter in the cocrystals than in  $\beta$ -caffeine (except for 2C-OA). Then given that a TB contraction is expected to *increase*  $\delta_C^8$ ,<sup>48,49</sup> positive values of  $\Delta_C^8$  are anticipated throughout all cocrystals, in stark contrast to the *de facto* observed experimental and modeled results. The



lack of an even qualitative  $\Delta_C/\Delta r(\text{CH}_3 \cdots \text{O/N})$  correlation also applies to the  $^{13}\text{C}_6\text{H}_3$  site: again, the wide HB-distance range in  $\beta$ -caffeine (207–276 pm; Table S3, ESI<sup>†</sup>) relative to those of the cocrystals (223–249 pm) suggest minor effects on  $\Delta_C^6$ . Notably, however, the  $\text{C}_6\text{H}_3 \cdots \text{O}$  bond-lengths in the  $\beta$ -caffeine structure is *consistently shorter* than those of any cocrystal, from which *negative*  $\Delta_C^6$  values are predicted throughout,<sup>48,49</sup> in clear contradiction to our NMR and DFT results. Moreover, no correlation was observed for the set of  $^{13}\text{CH}_n$  chemical shifts against the TB angle (data not shown), despite wide  $\theta_{\text{TB}}$  ranges within  $71^\circ$ – $90^\circ$  (4  $\delta_C^1$  values) and  $147^\circ$ – $178^\circ$  (8  $\delta_C^1$  values).

Notwithstanding the uncertainties accompanying (i)–(iii) above, we believe that our  $^{13}\text{C}$  chemical-shift data suggest that a TB-length contraction may *not necessarily* produce an increased  $^{13}\text{C}$  chemical shift, along previous difficulties to establish a general  $\delta_C^1/r(\text{CH}_3 \cdots \text{O/N})$  correlation. Such a relationship is likely obscured for similar reasons as some inconclusive experimental  $\delta_C^1/r(\text{CH}_n \cdots \text{O})$  correlations, for which  $^{13}\text{C}$  shift-alterations upon  $\text{CH} \cdots \text{O}$  bond formation depend both on the precise molecular fragments involved and (longer-range) crystal-structure effects,<sup>44,45</sup> whose complex interplay may result in  $^{13}\text{C}$  deshielding,<sup>44,46</sup> shielding,<sup>43</sup> or either/both.<sup>42,44</sup>

## 5 Conclusion

The present comprehensive NMR/DFT study encompassed altogether 68 distinct  $^{13}\text{C}$  sites and 33 unique  $^1\text{H}$  resonances from altogether four caffeine-based cocrystals and their six precursor structures, with an overall very good agreement between the experimental and modeled chemical shifts. We believe that the results herein may serve as accurate benchmark values for further MAS NMR investigations, given the very good accordance with previous literature for the  $^1\text{H}/^{13}\text{C}$  chemical shifts—such as the  $\delta_C$  data of 2C-MA and C-GA of ref. 50 along with both  $^1\text{H}$  and  $^{13}\text{C}$  chemical shifts of the diacid precursors—and because a significant fraction of all  $\delta_H/\delta_C$  data are presented herein for the first time.

Despite our large  $^{13}\text{C}$  and  $^1\text{H}$  chemical-shift ensembles and an encouraging NMR/DFT agreement, the herein established linear chemical-shift/distance correlations were confined to the  $\text{COO}^1\text{H} \cdots \text{O/N}$  diacid–diacid and diacid–caffeine hydrogen bonds, along with the  $\text{COO}^1\text{H} \cdots \text{N}$  counterparts, which nonetheless are those most instrumental for the supramolecular cocrystal organization. We also examined possible  $\text{CH}_3 \cdots \text{O/N}$  tetrel-bond effects on the  $^1\text{H}/^{13}\text{C}$  chemical shifts, which were overall uncertain and inconclusive but suggesting that previously reported (weak) chemical-shift correlations against tetrel-bond parameters might not hold in general, thereby underscoring the need for more research in this very sparsely investigated field. Further efforts towards better confining the H-atom positions of the caffeine–diacid cocrystals by direct  $^1\text{H}$ – $^1\text{H}$  and  $^1\text{H}$ – $^{13}\text{C}$  internuclear-distance measurements are underway by employing a recent NMR crystallography method.<sup>81,82</sup>

Except for the methylene groups of MA/GA and their cocrystals, the compromised  $^1\text{H}$  NMR spectral resolution (and for  $\beta$ –

caffeine also the  $^{13}\text{C}$  NMR counterpart) originates mainly from chemical-shift dispersions stemming from anisotropic bulk magnetic susceptibility and structural disorder rather than the often dominant peak-broadening from  $^1\text{H}$ – $^1\text{H}$  interactions. Hence, modest spectral resolution enhancements are expected from faster-MAS ( $> 60$  kHz)  $^1\text{H}$  NMR experiments, and let alone by utilizing higher fields ( $B_0 > 14.1$  T) because the shift-dispersion scales linearly with  $B_0$ . That sharply contrasts with the  $^{13}\text{C}$  NMR scenario, however, where  $B_0 \geq 14.1$  T experimentation appears mandatory for resolving all 10 resonances from the 8 distinct  $^{13}\text{C}$  sites of anhydrous  $\beta$ -caffeine, where the previously unassigned  $^{13}\text{C}$  NMR peaks at 30.2 ppm (C7/C8) and 149.0 ppm (C3) are spectral markers for discriminating the disordered anhydrous  $\beta$ -caffeine polymorph from both its disordered  $\alpha$ -caffeine and ordered hydrated  $\text{C}\cdot\text{H}_2\text{O}$  counterparts. This insight facilitates further  $\alpha$ – $\beta$ -phase quantifications of mixtures of both polymorphs by  $^{13}\text{C}$  MAS NMR alone, which has hitherto only proven possible by PXRD analyses.

## Conflicts of interest

There are no conflicts to declare.

## Acknowledgements

This work was supported by the Knut and Alice Wallenberg Foundation (project 2019.0124), and in part by the Swedish Research Council (project VR 2022-03652). The computations were enabled by resources provided by the National Academic Infrastructure for Supercomputing in Sweden (NAISS), partially funded by the Swedish Research Council through grant agreement no. 2022-06725. We thank an anonymous reviewer for helpful comments on NMR-peak broadening factors.

## References

- 1 H. G. Brittain, Cocrystal systems of pharmaceutical interest: 2010, *Cryst. Growth Des.*, 2012, **12**, 1046–1054.
- 2 R. Shaikh, R. Singh, G. M. Walker and D. M. Croker, Pharmaceutical cocrystal drug products: an outlook on product development, *Trends Pharmacol. Sci.*, 2018, **39**, 1033–1048.
- 3 G. Bolla, B. Sarma and A. K. Nangia, Crystal engineering of pharmaceutical cocrystals in the discovery and development of improved drugs, *Chem. Rev.*, 2022, **122**, 11514–11603.
- 4 T. Friščić and W. Jones, Recent advances in understanding the mechanism of cocrystal formation via grinding, *Cryst. Growth Des.*, 2009, **9**, 1621–1637.
- 5 M. Rodrigues, B. Baptista, J. A. Lopes and M. C. Sarraguça, Pharmaceutical cocrystallization techniques. Advances and challenges, *Int. J. Pharm.*, 2018, **547**, 404–420.
- 6 U. J. Griesser and A. Burger, The effect of water vapor pressure on desolvation kinetics of caffeine 4/5-hydrate, *Int. J. Pharm.*, 1995, **120**, 83–93.



7 H. G. M. Edwards, E. Lawson, M. de Matas, L. Shields and P. York, Metamorphosis of caffeine hydrate and anhydrous caffeine, *J. Chem. Soc., Perkin Trans.*, 1997, **2**, 1985–1990.

8 A. V. Trask, W. D. S. Motherwell and W. Jones, Pharmaceutical cocrystallization: engineering a remedy for caffeine hydration, *Cryst. Growth Des.*, 2005, **5**, 1013–1021.

9 C. W. Lehmann and F. Stowasser, The crystal structure of anhydrous  $\beta$ -caffeine as determined from X-ray powder-diffraction data, *Chem. – Eur. J.*, 2007, **13**, 2908–2911.

10 K. Guo, G. Sadiq, C. Seaton, R. Davey and Q. Yin, Cocrystallization in the caffeine/maleic acid system: lessons from phase equilibria, *Cryst. Growth Des.*, 2010, **10**, 268–273.

11 T. Leyssens, G. Springuel, R. Montis, N. Candoni and S. Veesler, Importance of solvent selection for stoichiometrically diverse cocrystal systems: Caffeine/maleic acid 1:1 and 2:1 cocrystals, *Cryst. Growth Des.*, 2012, **12**, 1520–1530.

12 V. S. Mandala, S. J. Loewus and M. A. Mehta, Monitoring cocrystal formation via in situ solid-state NMR, *J. Phys. Chem. Lett.*, 2014, **5**, 3340–3344.

13 M. Mukaida, K. Sugano and K. Terada, Stability order of caffeine co-crystals determined by co-crystal former exchange reaction and its application for the validation of *in silico* models, *Chem. Pharm. Bull.*, 2015, **63**, 18–24.

14 K. P. Nartowski, Y. Z. Khimyak and D. J. Berry, Tuning the spontaneous formation kinetics of caffeine: malonic acid co-crystals, *CrystEngComm*, 2016, **18**, 2617–2620.

15 S. P. Brown, Probing proton-proton proximities in the solid state, *Prog. Nucl. Magn. Reson. Spectrosc.*, 2007, **50**, 199–251.

16 T. Le Marchand, T. Schubeis, M. Bonaccorsi, P. Paluch, D. Lalli, A. J. Pell, L. B. Andreas, K. Jaudzems, J. Stanek and G. Pintacuda,  $^1\text{H}$ -detected biomolecular NMR under fast magic-angle spinning, *Chem. Rev.*, 2022, **122**, 9943–10018.

17 M. K. Dudek, S. Kazmierski, M. Kostrzewska and M. J. Potrzebowski, Solid-state NMR studies of molecular crystals, *Annu. Rep. NMR Spectrosc.*, 2018, **95**, 1–81.

18 I. Schnell, Dipolar recoupling in fast-MAS solid-state NMR spectroscopy, *Prog. Nucl. Magn. Reson. Spectrosc.*, 2004, **45**, 145–207.

19 P. Hodgkinson, NMR crystallography of molecular organics, *Prog. Nucl. Magn. Reson. Spectrosc.*, 2020, **118–119**, 10–53.

20 M. Li, W. Xu and Y. Su, Solid-state NMR spectroscopy in pharmaceutical sciences, *Trac., Trends Anal. Chem.*, 2021, **135**, 116152.

21 M. Edén, Probing oxide-based glass structures by solid-state NMR: opportunities and limitations, *J. Magn. Reson. Open*, 2023, **16–17**, 100112.

22 G. D. Enright, V. V. Terskikh, D. H. Brouwer and J. A. Ripmeester, The structure of two anhydrous polymorphs of caffeine from single-crystal diffraction and ultrahigh-field solid-state  $^{13}\text{C}$  NMR spectroscopy, *Cryst. Growth Des.*, 2007, **7**, 1406–1410.

23 S. Bordignon, P. C. Vioglio, E. Priola, D. Voinovich, R. Gobetto, Y. Nishiyama and M. R. Chierotti, Engineering codrug solid forms: mechanochemical synthesis of an indomethacin-caffeine system, *Cryst. Growth Des.*, 2017, **17**, 5744–5752.

24 H. E. Kerr, H. E. Mason, H. A. Sparkes and P. Hodgkinson, Testing the limits of NMR crystallography: the case of caffeine-citric acid hydrate, *CrystEngComm*, 2016, **18**, 6700–6707.

25 S. Bhattacharya, Thermal expansion and dimensionality of a hydrogen bond network: a case study on dimorphic oxalic acid, *CrystEngComm*, 2020, **22**, 7896–7902.

26 N. Casati, P. Macchi and A. Sironi, Hydrogen migration in oxalic acid di-hydrate at high pressure?, *Chem. Commun.*, 2009, 2679–2681.

27 S. Bhattacharya, V. G. Saraswatula and B. K. Saha, Thermal expansion in alkane diacids—another property showing alternation in an odd–even series, *Cryst. Growth Des.*, 2013, **13**, 3651–3656.

28 V. R. Thalladi, M. Nusse and R. Boese, The melting point alternation in  $\alpha,\omega$ -alkanedicarboxylic acids, *J. Am. Chem. Soc.*, 2000, **122**, 9227–9236.

29 D. Rychkov, S. Arkhipov and E. Boldyreva, Structure-forming units of amino acid maleates. Case study of L-valinium hydrogen maleate, *Acta Crystallogr.*, 2016, **B72**, 160–163.

30 F. Mauri, B. G. Pfrommer and S. G. Louie, *Ab initio* theory of NMR chemical shifts in solids and liquids, *Phys. Rev. Lett.*, 1996, **77**, 5300–5303.

31 C. J. Pickard and F. Mauri, All-electron magnetic response with pseudopotentials: NMR chemical shifts, *Phys. Rev. B: Condens. Matter Mater. Phys.*, 2001, **63**, 245101.

32 T. Charpentier, The PAW/GIPAW approach for computing NMR parameters: a new dimension added to NMR of solids, *Solid State Nucl. Magn. Reson.*, 2011, **40**, 1–20.

33 C. Bonhomme, C. Gervais, F. Babonneau, C. Coelho, F. Pourpoint, T. Azaïs, S. E. Ashbrook, J. M. Griffin, J. R. Yates, F. Mauri and C. J. Pickard, First-principles calculation of NMR parameters using the gauge including projector augmented wave method: a chemist's point of view, *Chem. Rev.*, 2012, **112**, 5733–5779.

34 R. K. Harris, P. Jackson, L. H. Merwin, B. J. Say and G. Hägele, Perspectives in high-resolution solid-state nuclear magnetic resonance, with emphasis on combined rotation and multiple-pulse spectroscopy, *J. Chem. Soc., Faraday Trans. 1*, 1988, **84**, 3649–3672.

35 U. Sternberg and E. Brunner, The influence of short-range geometry on the chemical shift of protons in hydrogen bonds, *J. Magn. Reson., Ser. A*, 1994, **108**, 142–150.

36 N. R. Jagannathan, Carbon-13 chemical shielding tensors in alkanedicarboxylic acids. Influence of molecular geometry on the carboxyl carbon tensors in alkanedicarboxylic acids and related compounds, *Magn. Reson. Chem.*, 1989, **27**, 941–946.

37 Z. Gu and A. McDermott, Chemical shielding anisotropy of protonated and deprotonated carboxylates in amino acids, *J. Am. Chem. Soc.*, 1993, **115**, 4282–4285.

38 Z. Gu, R. Zambrano and A. McDermott, Hydrogen bonding of carboxyl groups in solid-state amino acids and peptides: comparison of chemical shielding, infrared frequencies, and structures, *J. Am. Chem. Soc.*, 1994, **116**, 6368–6372.



39 R. Gobetto, C. Nervi, M. R. Chierotti, D. Braga, L. Maini, F. Grepioni, R. K. Harris and P. Hodgkinson, Hydrogen bonding and dynamic behaviour in crystals and polymorphs of dicarboxylic-diamine adducts: a comparison between NMR parameters and x-ray diffraction studies, *Chem. – Eur. J.*, 2005, **11**, 7461–7471.

40 X. Xue and M. Kanzaki, Proton distributions and hydrogen bonding in crystalline and glassy hydrous silicates and related inorganic materials: insights from high-resolution solid-state nuclear magnetic resonance spectroscopy, *J. Am. Ceram. Soc.*, 2009, **92**, 2803–2830.

41 F. G. Vogt, J. S. Clawson, M. Strohmeier, A. J. Edwards, T. N. Pham and S. A. Watson, Solid-state NMR analysis of organic cocrystals and complexes, *Cryst. Growth Des.*, 2009, **9**, 2620–2626.

42 S. Scheiner, Identification of spectroscopic patterns of CH···O H-bonds in proteins, *J. Phys. Chem. B*, 2009, **113**, 10421–10427.

43 J. R. Yates, T. N. Pham, C. J. Pickard, F. Mauri, A. M. Armado, A. M. Gil and S. P. Brown, An investigation of weak CH···O hydrogen bonds in maltose anomers by a combination of calculation and solid-state NMR spectroscopy, *J. Am. Chem. Soc.*, 2005, **127**, 10216–10220.

44 A.-C. Uldry, J. M. Griffin, J. R. Yates, M. Pérez-Torralba, M. D. Santa María, A. L. Webber, M. L. L. Beaumont, A. Samoson, R. M. Claramunt, C. J. Pickard and S. P. Brown, Quantifying weak hydrogen bonding in uracil and 4-cyano-4'-ethynylphenyl: a combined computational and experimental investigation of NMR chemical shifts in the solid state, *J. Am. Chem. Soc.*, 2008, **130**, 945–954.

45 K. Bouzková, M. Babinský, L. Novosadová and R. Marek, Intermolecular interactions in crystalline theobromine as reflected in electron deformation density and  $^{13}\text{C}$  NMR chemical shift tensors, *J. Chem. Theory Comput.*, 2013, **9**, 2629–2638.

46 S. A. Southern and D. L. Bryce, To what extent do bond length and angle govern the  $^{13}\text{C}$  and  $^1\text{H}$  NMR response to weak CH···O hydrogen bonds? A case study of caffeine and theophylline cocrystals, *Solid State Nucl. Magn. Reson.*, 2022, **119**, 101795.

47 A. Bauzá, T. J. Mooibroek and A. Frontera, Tetrel-bonding interaction: rediscovered supramolecular force?, *Angew. Chem., Int. Ed.*, 2013, **52**, 12317–12321.

48 S. Scheiner, Ability of IR and NMR spectral data to distinguish between a tetrel bond and a hydrogen bond, *J. Phys. Chem. A*, 2018, **122**, 7852–7862.

49 S. A. Southern, M. S. West, M. J. Z. Bradshaw and D. L. Bryce, Experimental  $^{13}\text{C}$  and  $^1\text{H}$  solid-state NMR response in weakly tetrel-bonded methyl groups, *J. Phys. Chem. C*, 2021, **125**, 2111–2123.

50 N. J. Vigilante and M. A. Mehta, A  $^{13}\text{C}$  solid-state NMR investigation of four cocrystals of caffeine and theophylline, *Acta Crystallogr.*, 2017, **C73**, 234–243.

51 A. Coelho, *TOPAS-academic v6*, Coelho Software, 2016.

52 G. Metz, X. L. Wu and S. O. Smith, Ramped-amplitude cross polarization in magic-angle-spinning NMR, *J. Magn. Reson., Ser. A*, 1994, **110**, 219–227.

53 B. M. Fung, A. K. Khitrin and K. Ermolaev, An improved broadband decoupling sequence for liquid crystals and solids, *J. Magn. Reson.*, 2000, **142**, 97–101.

54 E. Leonova, A. S. Hakeem, K. Jansson, B. Stevensson, Z. Shen, J. Grins, S. Esmaeilzadeh and M. Edén, Nitrogen-rich La–Si–Al–O–N oxynitride glass structures probed by solid state NMR, *J. Non-Cryst. Solids*, 2008, **354**, 49–60.

55 S. J. Clark, M. D. Segall, C. J. Pickard, P. J. Hasnip, M. I. J. Probert, K. Refson and M. C. Payne, First principles methods using CASTEP, *Z. Kristallogr.*, 2005, **220**, 567–570.

56 J. P. Perdew and A. Zunger, Self-interaction correction to density-functional approximations for many-electron systems, *Phys. Rev. B: Condens. Matter Mater. Phys.*, 1981, **23**, 5048–5079.

57 J. R. Yates, C. J. Pickard and F. Mauri, Calculation of NMR chemical shifts for extended systems using ultrasoft pseudopotentials, *Phys. Rev. B: Condens. Matter Mater. Phys.*, 2007, **76**, 024401.

58 M. C. Payne, M. P. Teter, D. C. Allan, T. A. Arias and J. D. Joannopoulos, Iterative minimization techniques for *ab initio* total-energy calculations: molecular dynamics and conjugate gradients, *Rev. Mod. Phys.*, 1992, **64**, 1045–1097.

59 A. Tkatchenko and M. Scheffler, Accurate molecular van der Waals interactions from ground-state electron density and free-atom reference data, *Phys. Rev. Lett.*, 2009, **102**, 073005.

60 H. J. Monkhorst and J. D. Pack, Special points for Brillouin-zone integrations, *Phys. Rev. B: Solid State*, 1976, **13**, 5188–5192.

61 M. M. Maricq and J. S. Waugh, NMR in rotating solids, *J. Chem. Phys.*, 1979, **70**, 3300–3316.

62 U. Haeberlen, *High Resolution NMR in Solids. Selective Averaging*, Academic Press, New York, 1976.

63 J. Mason, Conventions for the reporting of nuclear magnetic shielding (or shift) tensors suggested by participants in the NATO ARW on NMR shielding constants at the University of Maryland, College Park, July 1992, *Solid State Nucl. Magn. Reson.*, 1993, **2**, 285–288.

64 C. López, R. Claramunt and J. Elguero, Oxalic acid/phenols and oxalic acid/cholesterol co-crystals: a solid state  $^{13}\text{C}$  CPMAS NMR study, *ARKIVOC*, 2008, 33–46.

65 E. Pindelska, A. Sokal, L. Szeleszczuk, D. M. Pisklak and W. Kolodziejki, Solid-state NMR studies of theophylline cocrystals with dicarboxylic acids, *J. Pharm. Biomed. Anal.*, 2014, **100**, 322–328.

66 J. Kastelic, Ž. Hodnik, P. Šket, J. Plavec, N. Lah, I. Leban, M. Pajk, O. Planinšek and D. Kikelj, Fluconazole cocrystals with dicarboxylic acids, *Cryst. Growth Des.*, 2010, **10**, 4943–4953.

67 M. Ilczyszyn, D. Godzisz and M. M. Ilczyszyn, Sarcosine-maleic acid (1:1) crystal: structure,  $^{13}\text{C}$  NMR and vibrational properties, protonation character, *Spectrochim. Acta, Part A*, 2003, **59**, 1815–1828.

68 Nonappa and E. Kolehmainen, Caffeine as a gelator, *Gels*, 2016, **2**, 9.

69 J. Słtkowski, L. Stefaniak, L. Nicol, M. L. Martin, G. J. Martin and G. A. Webb, Complete assignments of  $^1\text{H}$ ,  $^{13}\text{C}$ , and  $^{15}\text{N}$



NMR spectra of caffeine, *Spectrochim. Acta, Part A*, 1995, **51**, 839–2841.

70 N. Liédana, A. Galve, C. Rubio, C. Téllez and J. Coronas, CAFZIF-8: one-step encapsulation of caffeine in MOF, *ACS Appl. Mater. Interfaces*, 2012, **4**, 5016–5021.

71 D. L. VanderHart, W. L. Earl and A. N. Garroway, Resolution in  $^{13}\text{C}$  NMR of organic solids using high-power proton decoupling and magic-angle sample spinning, *J. Magn. Reson.*, 1981, **44**, 361–401.

72 M. Alla and E. Lippmaa, Resolution limits in magic-angle rotation NMR spectra of polycrystalline solids, *Chem. Phys. Lett.*, 1982, **87**, 30–33.

73 A. J. Robbins, W. T. K. Ng, D. Jochym, T. W. Keal, S. J. Clark, D. J. Tozer and P. Hodgkinson, Combining insights from solid-state NMR and first principles calculation: applications to the  $^{19}\text{F}$  NMR of octafluoronaphthalene, *Phys. Chem. Chem. Phys.*, 2007, **9**, 2389–2396.

74 M. P. Hanrahan, A. Venkatesh, S. L. Carnahan, J. L. Calahan, J. W. Lubach, E. J. Munson and A. J. Rossini, Enhancing the resolution of  $^1\text{H}$  and  $^{13}\text{C}$  solid-state NMR spectra by reduction of anisotropic bulk magnetic susceptibility broadening, *Phys. Chem. Chem. Phys.*, 2017, **19**, 28153–28162.

75 J. G. Hexem, M. H. Frey and S. J. Opella, Molecular and structural information from  $^{14}\text{N}$ – $^{13}\text{C}$  NMR spectra of solids, *J. Chem. Phys.*, 1982, **77**, 3847–3856.

76 A. C. Olivieri, L. Frydman and L. E. Diaz, A simple approach for relating molecular structural information to the dipolar coupling in  $^{13}\text{C}$ – $^{14}\text{N}$  CP MAS NMR, *J. Magn. Reson.*, 1987, **75**, 50–62.

77 B. Berglund and R. W. Vaughan, Correlations between proton chemical shift tensors, deuterium quadrupole couplings, and bond distances in solids, *J. Chem. Phys.*, 1980, **73**, 2037–2043.

78 R. G. Griffin and D. J. Ruben, Carbon-13 chemical shielding in ammonium hydrogen oxalate hemihydrate, *J. Chem. Phys.*, 1975, **63**, 1272–1275.

79 R. G. Griffin, A. Pines, S. Pausak and J. S. Waugh,  $^{13}\text{C}$  chemical shielding in oxalic acid, oxalic acid dihydrate, and diammonium oxalate, *J. Chem. Phys.*, 1975, **63**, 1267–1271.

80 C. Gardiennet-Doucet, X. Assfeld, B. Henry and P. Tekely, Revealing successive steps of deprotonation of L-phosphoserine through  $^{13}\text{C}$  and  $^{31}\text{P}$  chemical shielding tensor fingerprints, *J. Phys. Chem. A*, 2006, **110**, 9137–9144.

81 R. Mathew, B. Stevensson and M. Edén, Refined structures of O-phospho-L-serine and its calcium salt by new multi-nuclear solid-state NMR crystallography methods, *J. Phys. Chem. B*, 2021, **125**, 10985–11004.

82 Y. Yu, B. Stevensson, M. Pujari-Palmer, H. Guo, H. Engqvist and M. Edén, The monetite structure probed by advanced solid-state NMR experimentation at fast magic-angle spinning, *Int. J. Mol. Sci.*, 2019, **20**, 6356.

